Beyond the suprachiasmatic nucleus: circadian rhythmicity shapes astrocyte morphology and neuronal function in hippocampal area CA1

John P. McCauley[1], Maurice A. Petroccione[1], Lianna Y. D'Brant[1,2], Gabrielle C. Todd[1], Nurat Affinnih[1], Justin J. Wisnoski[1], Shergil Zahid[1], Swasti Shree[1,3], Alioscka A. Sousa[4,5], Rosanna Migliore[6], Alexey Brazhe[7,8], Richard D. Leapman[5], Alexander Khmaladze[2], Alexey Semyanov[8,9], Michele Migliore[6] and Annalisa Scimemi[1]

[1] SUNY Albany, Department of Biology,
1400 Washington Avenue, Albany (NY) 12222, USA
[2] SUNY Albany, Department of Physics,
1400 Washington Avenue, Albany (NY) 12222, USA
[3] Bethlehem Central High School
700 Delaware Avenue, Delmar (NY) 12054, USA
[4] Federal University of São Paulo, Department of Biochemistry,
100 Rua Tres de Maio, São Paulo (SP) 04044-020, Brazil
[5] National Institute of Biomedical Imaging and Bioengineering, National Institutes of Health,
9000 Rockville Pike, Bethesda (MD) 20892, USA
[6] Institute of Biophysics, National Research Council,
153 Via Ugo la Malfa, Palermo (PA) 90146, Italy
[7] Lomonosov Moscow State University, Department of Biophysics,
Leninskie Street 1/12, Moscow 119234, Russia
[8] Department of Molecular Neurobiology, Institute of Bioorganic Chemistry,
Miklukho-Maklaya Street 16/10, Moscow 117997, Russia
[9] Sechenov First Moscow State Medical University,
Bolshaya Pirogovskaya Street 19c1, Moscow 119146, Russia

Abstract

Most animal species operate according to a 24-hour period set by the suprachiasmatic nucleus (SCN) of the hypothalamus. Despite the lack of direct synaptic connections to the hippocampus, the rhythmic activity of the SCN modulates memory-dependent processes in the hippocampus. What accounts for these effects has long remained unknown. Here, we show that there are cell-type specific structural and functional changes that take place in the hippocampus and that modulate the strength of excitatory synaptic transmission in area CA1 with circadian rhythmicity. Pyramidal neurons change the surface expression of NMDA receptors. Fine astrocytic processes glide through the neuropil, leading to changes in the time course of glutamate uptake and integration of temporally clustered excitatory synaptic inputs. These findings identify important mechanisms through which neurons and astrocytes modify the synaptic environment and contribute to the local storage of information in the hippocampus and the dynamics of learning and memory processing.

Introduction

The circadian rhythmicity with which mammals sleep, feed, regulate their body temperature and engage in reproductive behaviors is controlled by the main circadian master clock, the SCN of the hypothalamus, and by the coordinated activity of other semi-autonomous ancillary oscillators distributed in the brain and in peripheral tissues (Guilding and Piggins, 2007). Most neuronal projections from the SCN remain confined within the medial hypothalamus, and control the circadian release of corticosteroids into the bloodstream (i.e. gluococorticoids and mineralocorticoids) (Lehman et al., 1987; Meyer-Bernstein et al., 1999; Kalsbeek and Buijs, 2002). A few projections reach the inter-geniculate leaflet and paraventricular nucleus of the thalamus and are functionally important for the rhythmic production of melatonin by the pineal gland (Moore, 1996). Corticosteroids and melatonin have important regulatory effects, which take place through the activation of receptors expressed broadly in the brain and in peripheral organs (Reppert et al., 1996; Dubocovich et al., 2003; Dubocovich, 2007). The rhythmic control of gene and protein expression is fully established during embryonic development (Namihira et al., 1999; Reick et al., 2001; Wakamatsu et al., 2001; Sumova et al., 2012). The endogenous rhythmic activity of the SCN and of the pineal gland can be powerfully entrained by environmental cues, or zeitgebers, the most potent of which is light. By activating direct retino-hypothalamic glutamatergic connections, light evokes a fast-onset, sustained increase in the firing rate of SCN neurons, ultimately leading to reduced melatonin production and, in nocturnal animals, reduced glucocorticoid release (Moore and Lenn, 1972; Stephan and Zucker, 1972; Meijer et al., 1998; Ishida et al., 2005). Therefore, in mice, the production of glucocorticoids, mineralocorticoids and melatonin all peak during the dark phase of the circadian cycle (ZT12-24).

Interestingly, synaptically excitability in the hippocampus fluctuates during circadian rhythms (Barnes et al., 1977) and more than 10% of hippocampal genes and proteins show circadian fluctuations (Debski et al., 2017). Learning and memory formation, two functions that are conserved across species and that in mammals rely on the activity of the hippocampal formation, are also modulated by circadian rhythms (Ruby et al., 2008; Gerstner et al., 2009; Smarr et al., 2014; Shimizu et al., 2016; Snider et al., 2016; Rawashdeh et al., 2018). For example, behavioral studies indicate that mice trained to context fear conditioning protocols acquire the conditioning more slowly if trained during the dark (D) phase of the circadian cycle (ZT12-24) (Chaudhury and Colwell, 2002), a time when long-term plasticity is also reduced (Winson and Abzug, 1977, 1978). Interestingly, this circadian control of hippocampal function and plasticity is retained also in reduced slice preparations, as evidenced by the reduced magnitude of long-term potentiation (LTP) at hippocampal Schaffer collateral synapses in slices prepared during the D-phase (Harris and Teyler, 1983; Raghavan et al., 1999). The persistence of these effects in slices suggests that they are independent of the ongoing activity of extra-hippocampal inputs and might be due to the presence of one or more diffusible factors that are not easily washed out of slices, but whose identity has not been revealed. On one hand, increased glucocorticoid levels during the active phase of the circadian cycle are thought to facilitate memory formation and cognition (Hui et al., 2004; Yuen et al., 2011; Whitehead et al., 2013). On the other hand, melatonin has been proposed to be both sufficient and necessary for poor memory formation and plasticity during the D-phase (Ozcan et al., 2006; Rawashdeh et al., 2007).

The propensity of excitatory synapses to express LTP depends on their initial strength, which in turn is influenced by the density, composition and time course of activation of glutamate receptors (Migliore et al., 2015). Glutamate clearance relies on passive diffusion and active transport, mostly mediated by astrocytes' glutamate transporters GLAST and GLT-1. Since astrocytes are competent circadian oscillators (Prolo et al., 2005; Brancaccio et al., 2017; Brancaccio et al., 2019), and impaired glutamate uptake degrades LTP (Katagiri et al., 2001; Scimemi et al., 2009), we hypothesized that these cells, in addition to

neurons, might also contribute to circadian changes in hippocampal plasticity. Our data show that NMDA receptor activation is reduced during the D-phase, a time when astrocytes retract their fine processes from excitatory synapses and glutamate clearance is prolonged. These changes lead to decreased temporal summation of AMPA EPSPs and reduced LTP during the D-phase. Together, our data provide a new mechanistic understanding of the molecular and cellular mechanisms modulating daily changes in hippocampal plasticity.

Results

The hippocampus is a competent circadian oscillator

Central and peripheral circadian clocks are genetically equipped to generate rhythms during embryonic development, but continue their maturation during the first postnatal week. At P10, when synaptogenesis in the SCN and other peripheral oscillators is complete, rats show regular changes in their body temperature that are controlled by the rhythmic activity of circadian oscillators (Weinert, 2005; Sumova et al., 2008). We confirmed that this holds true also in juvenile mice aged P14–21, from which we measured the body temperature using micro-transponders implanted under the skin of the shoulder (**Fig. 1A-B**). Their mean body temperature (~35.8°C) displayed consistent oscillations of ±0.6°C, with detectable peaks at the end of the light (L)-phase (ZT12) and troughs at the end of the dark (D)-phase (ZT0). We confirmed that the expression of clock genes like *Arntl* and *Per2* in the mouse hippocampus is not limited to the SCN. Accordingly, using an RNAscope fluorescent in situ hybridization assay (**Fig. 1C-E**), we showed that *Per2* expression increased significantly in acute slices prepared at ZT15.5 (D-phase) compared to those prepared at ZT3.5 (L-phase) in the SCN (SCN_L: 2.9e-3±0.6e-3 (n=28), SCN_D: 14.8e-3±1.8e-3 (n=33), ***p=3.5e-7), the pyramidal cell layer of hippocampal area CA1 ($CA1\text{-}PC_L$: 30.1e-3±4.6e-3 (n=31), $CA1\text{-}PC_D$: 44.1e-3±3.9e-3 (n=36), *p=0.023) and *stratum radiatum* ($CA1\text{-}SR_L$: 1.1±0.2 (n=33), $CA1\text{-}SR_D$: 10.9±1.1 (n=32) ***p=2.4e-10). By contrast, the expression of *Arntl* did not change significantly between these two time points in any of the brain regions mentioned above (SCN_L: 4.2e-3±0.5e-3 puncta/μm^2 (n=28), SCN_D: 4.9e-3±1.1e-3 puncta/μm^2 (n=33), p=0.54; $CA1\text{-}PC_L$: 14.6e-3±1.6e-3 puncta/μm^2 (n=31), $CA1\text{-}PC_D$: 11.0e-3±1.9e-3 puncta/μm^2 (n=36), p=0.16; $CA1\text{-}SR_L$: 2.1e-3±0.5e-3 puncta/μm^2 (n=33), $CA1\text{-}SR_D$: 1.7±0.5 puncta/μm^2 (n=32), p=0.56). These findings are important because they support the notion that hippocampus, not just the SCN, is a competent circadian oscillator.

Circadian rhythmicity shapes long-term plasticity at Schaffer collateral synapses

Consistent with previous work, we also detected changes in the magnitude of theta burst stimulation-induced (TBS)-LTP at Schaffer collateral synapses, using a stimulation protocol that aims to mimic the endogenous electroencephalographic activity measured in the rodent hippocampus during exploratory learning tasks (Buzsaki, 2002). The TBS protocol induced LTP in slices prepared in the L-phase but not in those prepared in the D-phase (LTP_L: 1.17±0.03 ms^{-1} (n=14), ***p=3.9e-4; LTP_D: 0.97±0.06 ms^{-1} (n=7), p=0.64; **Fig. 1F-G**). This was not a photic effect, but rather a circadian one, because LTP could still be induced in slices prepared at ZT3.5 from mice kept under constant darkness conditions (LTP_{DD}: 1.14±0.03 ms-1 (n=14), **p=1.1e-3). The effect recorded from slices prepared in the D-phase was significantly different than the one observed in slices prepared in the L- and subjective L-phases (LTP_D vs LTP_L: *p=0.014; LTP_D vs LTP_{DD}: *p=0.029; **Fig. 1G**).

If the detected changes in LTP were due to circadian differences in the activation of corticosteroid and melatonin receptors, blocking them pharmacologically should not affect plasticity during the L-phase but should rescue it during the D-phase. The two main types of corticosteroids produced by the adrenal gland

are glucocorticoids and mineralocorticoids. Consistent with our hypothesis, blocking NR3C1 mineralocorticoid receptors with spironolactone (10 µM; LTP_L: 1.19±0.03 ms^{-1} (n=7), **p=1.4e-3) and blocking NR3C2 glucocorticoid receptors with mifepristone (1 µM; LTP_L: 1.17±0.02 ms^{-1} (n=8), ***p=1.9e-4) did not occlude LTP in slices prepared during the L-phase (**Fig. 2A,B**). C57BL/6 mice carry two mutations in biosynthetic enzymes for melatonin (Ebihara et al., 1986; Kasahara et al., 2010; Peirson et al., 2018) and MT1/2 melatonin receptor gene expression is low in the hippocampus (Saunders et al., 2018). Consistent with these findings, blocking MT1/2 melatonin receptors with luzindole (50 µM) in slices prepared during the L-phase did not occlude LTP (LTP_L: 1.16±0.04 ms^{-1} (n=11), **p=1.4e-3; **Fig. 2C**). No LTP was detected in the D-phase in the presence of luzindole (LTP_D: 1.05±0.04 ms^{-1} (n=7), p=0.22; **Fig. 2F**). By contrast, blocking NR3C1 (LTP_D: 1.13±0.02 ms^{-1} (n=8), ***p=5.9e-4) or NR3C2 receptors (1.23±0.04 ms^{-1} (n=8), ***p=9.1e-4) in slices prepared during the D-phase rescued LTP (**Fig. 2D,E**). These data not only confirm previous works showing that LTP expression is modulated during the circadian cycle, but also identify corticosteroids as key molecules responsible for this effect.

The activation of NMDA receptors on CA1 pyramidal cells varies with circadian rhythmicity

We performed experiments to determine whether the effects described above could be accounted by changes in pre- or post-synaptic function (**Fig. 3**). We alternated single and paired electrical stimuli (10-20 V, 50 µs) to evoke glutamate release from Schaffer collaterals. We recorded AMPA EPSCs using a Cs-based internal solution while keeping CA1 pyramidal cells at a holding potential of -65 mV, in the presence of the $GABA_A$ receptor antagonist picrotoxin (100 µM). After recording a stable baseline of AMPA EPSCs, we blocked them by bath applying the AMPA receptor antagonist NBQX (10 µM) and switched the holding potential to +40 mV to record NMDA EPSCs. Our measures of AMPA and NMDA EPSC paired-pulse ratio (PPR) remained similar during the L/D-phases, suggesting that there was no change in pre-synaptic release probability (AMPA PPR_L: 2.7±0.1 (n=19), AMPA PPR_D: 2.7±0.1 (n=13), p=0.98; NMDA PPR_L: 2.3±0.2, NMDA PPR_D: 2.6±0.3, p=0.62; **Fig. 3A,B**). In these experiments, the stimulus strength was set to evoke AMPA EPSCs of similar amplitude during the L/D-phases (AMPA EPSC amp_L: 72±7 pA, AMPA EPSC amp_D: 93±12 pA, p=0.15). Their rise time (AMPA EPSC $rise_L$: 1.9±0.1 ms, AMPA EPSC $rise_D$: 2.2±0.2 ms, p=0.15) and half decay time (AMPA EPSC t_{50L}: 10.0±0.4 ms, AMPA EPSC t_{50D}: 10.7±0.8 ms, p=0.47) were also similar, suggesting no change in the time course of AMPA receptor activation when deliverin single stimuli to Schaffer collaterals (**Fig. 3C,D**). The amplitude of the NMDA EPSCs, however, was smaller in the D-phase (NMDA EPSC amp_L: 94±15 pA, NMDA EPSC amp_D: 47±7 pA, **p=8.2e-3), with no change in their rise and half decay time (NMDA EPSC $rise_L$: 5.6±0.2 ms, NMDA EPSC $rise_D$: 5.8±0.4 ms, p=0.75; NMDA EPSC t_{50L}: 99±7 ms, NMDA EPSC t_{50D}: 101±7 ms, p=0.85; **Fig. 3E,F**). The reduced NMDA EPSC amplitude led to reduced NMDA/AMPA ratio in the D-phase, which had not been previously reported ($NMDA/AMPA_L$: 2.2±0.3, $NMDA/AMPA_D$: 1.0±0.2, **p=3.7e-3; **Fig.10G,H**). We confirmed these results in separate experiments in which RuBi-glutamate (100 µM) was superfused through the recording chamber and uncaged using a 5 ms duration light pulse generated by a SOLA-SE light engine (Lumencor, Beaverton, OR) and delivered to the sample by connecting the light source to the epi-fluorescence port of the microscope using a light guide (2.7 mW at the specimen plane; **Fig. 3I-L**). We recorded electrically-evoked and flash-evoked AMPA and NMDA EPSCs in the same cells. Once again, only the amplitude of electrically-evoked NMDA EPSCs was smaller during the D-phase (AMPA EPSC amp_L: 110±17 pA (n=5), AMPA EPSC amp_D: 73±19 pA (n=5), p=0.18; NMDA EPSC amp_L: 40±7 pA, NMDA EPSC amp_D: 13±5 pA, *p=0.017; **Fig. 3I,J**) as was that of flash-evoked NMDA EPSCs, not AMPA EPSCs (AMPA Flash-EPSC amp_L: 80±16 pA, AMPA Flash-EPSC amp_D: 112±25 pA, p=0.31; NMDA Flash-EPSC amp_L: 254±42 pA, NMDA Flash-EPSC amp_D: 69±28 pA, ***p=7.8e-3; **Fig. 3K,L**).

These effects were not associated with gross changes in the density of excitatory synaptic contacts onto CA1 pyramidal cells, as indicated by the presence of a similar spine density in dendrites from biocytin-filled neurons in slices prepared during the L/D-phases (L: 0.64±0.03 (n=85), D: 0.65±0.02 (n=105), p=0.90; **Fig. 4A-B**).

Circadian changes in astrocyte glutamate clearance affect the temporal summation of AMPA EPSCs

The results presented so far point to the existence of regulatory mechanisms that alter NMDA receptor activation and LTP expression at Schaffer collateral synapses onto CA1 pyramidal cells. A circadian reduction in the weight of NMDA currents is not expected to change the summation of AMPA or NMDA EPSCs evoked by temporally clustered stimuli, like those that compose each burst of the LTP-inducing TBS stimulation. Accordingly, the peak NMDA EPSC recorded when delivering trains of five pulses at 100 Hz to CA1-PCs was similar during the L/D-phases (**Fig. 5A**). Surprisingly, however, the summation of AMPA EPSCs was reduced in the D-phase (**Fig. 5A**). Using a kinetic model of AMPA and NMDA receptors we showed that these effects could be recapitulated if, in addition to the reduced activation of NMDA receptors in the D-phase, there is also a prolongation in the time course of the evoked extracellular glutamate concentration profile in the extracellular space. This would promote AMPA receptor desensitization, reducing the temporal summation of AMPA EPSCs. The effect on NMDA EPSCs would be marginal, because the desensitization rate of NMDA receptors is significantly lower compared to that of AMPA receptors (**Fig. 5B**). This hypothesis was supported by a multi-compartmental NEURON model that takes into account the complex morphology of CA1 pyramidal cells in the mouse hippocampus and the random spatial distribution of excitatory inputs through the apical dendritic tree in *stratum radiatum* (**Fig. 5C,D**). The model confirmed that the smaller AMPA EPSC summation in the D-phase can be accounted for by a 3-fold increase in the recovery rate of the peak conductance of these receptors (from 10 to 30 ms), consistent with an increased desensitization of AMPA receptors during the D-phase. The small reduction in NMDA EPSC summation during the D-phase was accounted for by a 15% reduction in the peak conductance of NMDA receptors (**Fig. 5C,D**). This is consistent with experimental data showing reduced NMDA receptor activation during the D-phase (**Fig. 3**). Together, these findings identify two important phenomena contributing to circadian changes in excitatory synaptic transmission in hippocampal area CA1.

A prolongation in the lifetime of synaptically-released glutamate in the extracellular space can lead to changes in the time course of synaptically-activated currents (STCs), which can be recorded from astrocytes using experimental and analytical tools that we and others have extensively characterized (Diamond, 2005; Scimemi et al., 2009; Scimemi and Diamond, 2013; Sweeney et al., 2017). Stimulation of excitatory Schaffer collaterals evokes glutamate release in *stratum radiatum*, and causes the onset of a complex current waveform in astrocytes (**Fig. 6A**). Because of the low resistance of the astrocytes' cell membrane, the first part of this current is a transient outward current corresponding to the extracellular fiber volley, a readout of action potentials travelling along Schaffer collaterals. This fiber volley is not followed by a field current generated by glutamate receptor activation, because all recordings were performed in the presence of AMPA and $GABA_A$ receptor blockers (NBQX 10 µM, picrotoxin 100 µM). What follows the fiber volley is an inward current representing the overlay of a sustained potassium current, through which astrocytes remove potassium ions accumulated in the extracellular space from action potential firing in neurons, and a glutamate transporter-mediated current (i.e. the STC) due to the coordinated movement of glutamate with Na^+, K^+ and H^+ across the membrane (Zerangue and Kavanaugh, 1996). As expected, small changes in the stimulation strength across cells led to proportionate changes in the amplitude of the fiber volley and of the potassium current (**Fig. 6B**). The range of stimulus intensity used in our experiments evoked STCs of similar amplitude and rise time, across the L/D-phases (STC amp_L: 25.0±3.1 pA (n=7), STC amp_D: 23.8±3.1 pA (n=7), p=0.79; STC $rise_L$: 1.5±0.2 ms (n=7), STC $rise_D$: 1.7±0.2 ms

(n=7), p=0.34; **Fig. 6C**). However, STCs decayed more slowly in the D-phase, as evidenced by measuring the half decay time (t_{50L}: 8.0±0.3 ms (n=7), t_{50D}: 11.9±0.8 (n=7), **p=2.2e-3) and the centroid ($<t>_L$: 8.5±0.4 ms (n=7), $<t>_D$: 14.3±1.3 ms (n=7), **p=3.6e-3; **Fig. 6C**). The kinetics of the STC are similar to those of the facilitated portion of the STC (fSTC), obtained by subtracting STCs evoked by single and paired stimulation (100 ms inter-pulse interval) (Diamond, 2005; Scimemi et al., 2009; Scimemi and Diamond, 2013; Scimemi et al., 2013; Sweeney et al., 2017). A low concentration of the broad spectrum glutamate transporter antagonist TFB-TBOA (1 μM) reduced the fSTC amplitude (norm fSTC amp_L: 0.43±0.05 (n=7) ***p=1.9e-5, norm fSTC amp_D: 0.49±0.06 (n=7), ***p=9.5e-5, L vs D: p=0.47) and prolonged its kinetics similarly during the L/D-phases (norm fSTC $rise_L$: 1.3±0.1 **p=2.3e-3, norm fSTC $rise_D$: 1.1±0.1, ***p=8.7e-4, L vs D: p=0.066; norm fSTC t_{50L}: 1.2±0.1, **p=7.8e-3, norm fSTC t_{50D}: 1.1±0.1, *p=0.017, L vs D: p=0.070; norm fSTC $<t>_L$: 1.2±0.1, *p=0.02, norm fSTC $<t>_D$: 1.1±0.1, *p=0.029, L vs D: p=0.097; **Fig. 6D**). The fSTCs are useful because they can be used to derive the time course of glutamate clearance from astrocytes (Diamond, 2005; Scimemi and Diamond, 2013; Sweeney et al., 2017). This analysis indicated that the time of glutamate clearance from astrocytic membranes is slower during the D-phase ($<t>_{clearanceL}$: 7.4±0.4 ms (n=7), $<t>_{clearanceD}$: 9.0±0.5 ms (n=7), L vs D: *p=0.035; **Fig. 6E,F**), suggesting that the glutamate uptake capacity of these cells varies physiologically at different times of the day.

These effects were not confounded by changes in the passive membrane properties of astrocytes across the L/D-phases (**Fig. 7**). The I/V plots, obtained by measuring the steady-state current response to 100 ms long voltage steps (**Fig. 7A**), showed a similar profile during the L/D-phases (**Fig. 7B**). The membrane resistance (R_{mL}: 25.0±1.5 MOhm (n=45), R_{mD}: 27.0±1.1 MOhm (n=40), p=0.28; **Fig. 7C-D**) and capacitance were also similar during the L/D-phases (C_{mL}: 12.0±1.1 pF (n=44), C_{mD}: 15.3±1.7 pF (39), p=0.11; **Fig. 7C-D**). These values were significantly lower than the membrane resistance and capacitance of CA1 pyramidal cells (R_{mL}: 255.6±32.2 MOhm (n=13), ***p=1.1e-5, R_{mD}: 201.0±17.8 MOhm (n=10), ***p=4.3e-6; C_{mL}: 56.0±5.5 pF (n=13), ***p=2.8e-6, C_{mD}: 50.9±7.1 pF (n=10), ***p=6.5e-4), which also did not differ significantly during the L/D-phases (R_{mL} vs R_{mD} p=0.15; C_{mL} vs C_{mD} p=0.57; **Fig. 7E**). The astrocytes' resting membrane potentials remained similar during the L/D-phases (V_{rL}: -82±4 mV (n=9), V_{rD}: -81±4 (n=6), p=0.88; **Fig. 7F**), as did their level of dye coupling, measured via confocal imaging of biocytin-filled cells ($coupling_L$: 12±2 (n=11), $coupling_D$: 12±1 (n=7), p=0.98; **Fig. 7F**).

Slower glutamate clearance in the D-phase was not due to reduced expression of the astrocyte glutamate transporters GLAST and GLT-1, which we measured in protein extracts from mouse hippocampi dissected at ZT3.5 or ZT15.5 using Western blotting (**Fig. 8**). Glutamate transporters assemble as trimers that can only be partially broken into monomers and dimers during SDS-PAGE. Thus, the total band intensity of GLAST monomers and dimers, normalized to the band intensity of our loading control β-actin, was 1.49±0.13 (n=20) during the L-phase and 1.33±0.17 (n=20) during the D-phase (p=0.47; **Fig. 8A,B**), representing a non-significant 11±8% reduction of GLAST expression during the D-phase (p=0.30; **Fig. 8C**). Similarly, the total normalized band intensity of GLT-1 was 0.77±0.08 (n=16) during the L-phase and 0.78±0.06 (n=16) during the D-phase (p=0.90; **Fig. 8D-E**), leading to a non-significant 3±6% change of expression during the D-phase (p=0.78; **Fig. 8F**).

The gross structure of the hippocampal neuropil does not change during the circadian cycle

Other potential mechanisms that could account for the slower glutamate clearance during the D-phase are widespread changes in the structure of the neuropil (i.e. cell swelling) or more subtle, local rearrangements of the synaptic environment, which we previously documented (Sweeney et al., 2017). We analyzed the overall cell membrane and cytoplasm composition of hippocampal slices prepared at ZT3.5 and ZT15.5 using a marker-free holo-tomographic approach, which allowed us to distinguish plasma

membranes from cytoplasmic compartments based on differences in their refractive-index gradient (Cotte et al., 2013). We confirmed that this technique can be used to resolve widespread changes in the plasma membrane/cytoplasm (M/C) ratio in hippocampal area CA1 (**Fig. 9**). To do this, we prepared acute hippocampal slices and stored them for one hour in saline solutions of different osmolality that are known to induce cell swelling or shrinkage (**Fig. 9A-D**). We then fixed the slices, mounted them on slides and collected z-stacks using the 3D Cell Explorer digital holo-tomographic microscope (Nanolive, Ecublens, Switzerland). Plasma membranes and cytoplasmic compartments were detected and digitally stained using the refractive index values and gradients shown in **Fig. 9B**. The M/C ratio, calculated as the ratio between the number of voxels that labelled plasma membranes (yellow) and cytoplasm (magenta), provides a readout of the surface area-to-volume ratio of cell processes in hippocampal area CA1. As expected, the M/C ratio increased with increasing osmolality and induced cell shrinkage (**Fig. 9C,D**). There was a tight correlation between changes in the M/C ratio and changes in osmolality in both the pyramidal cell layer (**Fig. 9C**) and *stratum radiatum*, where the M/C ratio was larger due to the absence of cell bodies (**Fig. 9D**). Having confirmed the sensitivity of this imaging technique, we used it to measure the M/C ratio in slices prepared during the L/D-phases. The parameters used to label the plasma membrane and cytoplasm during the L/D-phases were similar among each other and with respect to those used in the osmolality experiments (**Fig 9B,F**). We used them to measure the M/C ratio in *stratum radiatum*, the domain of area CA1 that contains most astrocytes and excitatory synapses (**Fig. 9E-G**). The lack of difference between the measures obtained during the L/D-phases suggests that no major cell swelling/shrinking occurs in *stratum radiatum* during the L/D-phases. (M/C $ratio_L$: 0.13±0.02 (n=12), M/C $ratio_D$: 0.10±0.02 (n=14), p=0.27).

Though valuable, this analysis cannot identify cell-specific structural changes that might occur only in astrocytes. To test whether changes in the overall structure of astrocytes occur during the L/D-phases, we acquired confocal images of biocytin-filled astrocytes and analyzed their maximal intensity projections before and after protein-retention expansion microscopy (proExM), a technique originally developed by Tillberg et al., 2016. Using proExM, we can isotropically expand biocytin-filled astrocytes and overcome a caveat of confocal microscopy applied to astrocyte imaging: the spatial resolution of confocal microscopy can be larger than the size of astrocytes' distal processes ($res_{x,y}=\lambda/2\cdot NA=488/2\cdot 1.4=174$ nm). We subjected hippocampal slices collected at Zt3.5 and ZT15.5 to three, 15 min rounds of expansion (**Fig. 10A**), which lead to a roughly 3.5-fold increase in slice area (norm $area_L$: 3.4±0.3 (n=6), norm $area_D$: 3.5±0.1 (n=6), p=0.84; **Fig. 10B-D**) and a 2-fold increase in slice perimeter (norm $perimeter_L$: 1.8±0.1 (n=6), norm $perimeter_D$: 1.9±0.1 (n=6), p=0.57; **Fig. 10E-G**). Before expansion, the biocytin-filled astrocytes imaged by confocal microscopy showed similar surface area during the L/D-phases ($area_L$: 3,891±478 μm^2 (n=15), $area_D$: 3,961±224 μm^2 (n=17), p=0.90; **Fig. 11A,C,E,G**). We imaged astrocytes processed using proExM using two-photon laser scanning microscopy. Even in this case, we found no difference in the average surface area of astrocytes during the L/D-phases ($area_L$: 26,400±3,680 μm^2 (n=9), $area_D$: 25,200±3,888 μm^2 (n=6), p=0.83; (**Fig. 11B,D,F,H**)), suggesting that the gross morphology of these cells does not change during the circadian cycle.

Astrocytes reduce the number of fine processes during the dark phase of the circadian cycle

The data outlined above do not rule out the occurrence of more subtle changes in astrocyte morphology, for example in the density of its smallest branches and/or in their proximity to excitatory synapses, which can be resolved using 3D axial STEM tomography (Sousa et al., 2011; Sweeney et al., 2017). We identified astrocytic processes in 5 µm wide, 1-1.5 µm thick tissue samples because of their lack of spines and clear cytoplasm, which distinguishes them from neurons. There were fewer astrocytic processes during the D-phase (**Fig. 12A,B**). Their volume and surface area did not change during the L/D-

phases (vol_L: 0.019±0.001 μm^3 (n=73), vol_D: 0.023±0.002 μm^3 (n=37), p=0.11; $area_L$: 0.78±0.04 μm^2 (n=73), $area_D$: 0.89±0.05 μm^2 (n=37) p=0.080; **Fig. 12C,D**). Because of this decrease in the number of astrocytic processes, the nearest neighbor distance between each post-synaptic density and their closest astrocyte process increased more than 2-fold from 155±18 nm (n=59) to 342±63 nm (n=28) during the L- and D-phases, respectively (**p=7.6e-3; **Fig. 12E**). These changes were not associated with changes in the size of the PSD regions (PSD $area_L$: 0.024±0.002 μm^2 (n=59), PSD $area_D$: 0.025±0.004 μm^2 (n=28), p=0.93; **Fig. 12F**).

A common way to analyze the number of dendritic branches formed by neurons relies on the use of Sholl analysis. This analysis is prone to errors when used on non-processed confocal images of astrocytes, because the multitude of fine processes of these cells confers them a fuzzy look. Recent image analysis approaches allow information about these fine, filamentous processes to be extracted using coherence-enhancing diffusion filtering (Weickert and Scharr, 2002) and an iterative convolution with oriented filters (see Methods). This procedure allowed a detailed visualization of astrocytic processes in confocal images (**Fig. 12G,H**). The Sholl analysis, applied to the processed confocal images, showed that the number of astrocytic intersections with circles of increasing radii centered on the soma decreased during the D-phase ($intersections_L$: 4,108±326 (n=26), $intersections_D$: 2,844±272 (n=20), **p=4.7e-3; **Fig. 12I,J**). An alternative method, not requiring image binarization, relies on the use of a shearlet multiscale framework (Guo and Labate, 2007) and provides an optimal approximation of anisotropic features like astrocytic process in confocal images (Brazhe, 2018). This method uses spatial entropy (H) and complexity (C) measures to describe the orderliness and feature-preferred orientation of an image, respectively (Brazhe, 2018; Gavrilov et al., 2018). In our analysis, we normalized the values of spatial entropy and complexity measured in the area covered by the biocytin-filled neuron by the values obtained in the adjacent neuropil. Consistent with the Sholl analysis, the normalized entropy was smaller during the D-phase (L: 0.935±0.003 (n=29), D: 0.924±0.002 (n=16), *p=0.037; **Fig. 12K**). These results support the 3D axial STEM data and indicate that astrocytes remodel their processes continuously during the circadian cycle.

Discussion

The results presented in this manuscript provide direct evidence for the existence of a circadian modulation of excitatory synaptic transmission within the hippocampus (**Fig. 1**), due to structural and functional remodeling of the synaptic environment. Neurons and astrocytes both contribute to this phenomenon, though in different ways. Neurons alter the size of the functional pool of glutamate NMDA receptors at the synapse (**Fig. 3**). Astrocytes change the number and proximity of their fine processes with respect to excitatory synapses (**Fig. 12**). The remodeling of astrocytes alters the time course of glutamate clearance from the extracellular space (**Fig. 6**). Although this does not have notable consequences on glutamate receptor activation during sparse synaptic stimulation, it profoundly alters the temporal summation of recurring stimuli and long-term plasticity (**Fig. 1,5**).

Astrocytes, neurons and the values of an ever-changing brain

Modifications of the synaptic environment are critical for information coding in the brain, and provide an important substrate for circuit plasticity. The shape, size and turnover of dendritic spines can be controlled in an activity-dependent manner over time scales that range from seconds to hours, during development (Rakic et al., 1986; Holtmaat et al., 2005; Richards et al., 2005; Kwon and Sabatini, 2011), in response to LTP-inducing protocols (Engert and Bonhoeffer, 1999) and in the adult brain (Gilbert, 1998). Analogous activity-dependent phenomena of structural plasticity also occur in small protoplasmic

astrocytic processes that are commonly found around synapses (Reichenbach et al., 2010; Lavialle et al., 2011). Accordingly, different groups have reported that these fine processes can extend, retract, bud and glide through the neuropil (Hirrlinger et al., 2004; Haber et al., 2006). The distance over which these movements take place are comparable to the distance that spines can grow or shrink (i.e. hundreds of nm) and are therefore physiologically relevant. One of the reasons these movements are functionally important is that small changes in the relative proximity of astrocytic processes and spines have important consequences on the lifetime of glutamate in the extracellular space, its uptake, and ultimately for the regulation of the strength and timing of information transfer across neurons. Accordingly, suppressing astrocyte motility has been shown to impair the stabilization and maturation of synapses (Nishida and Okabe, 2007).

At excitatory glutamatergic synapses, multiple molecular mechanisms can lead to changes in the proximity of astrocytic processes to spines, which in turn contributes to modify the time course of glutamate receptor activation. For example, we previously showed that activating PAR1 G-protein coupled receptors leads to proliferation and closer apposition of astrocytic processes to excitatory synapses, leading to reduced AMPA and NMDA receptor activation (Sweeney et al., 2017). Since PAR1 receptors are typically activated by serine proteases in the bloodstream, we concluded that this movement of astrocytes towards synapses might be indicative of similar phenomena of structural plasticity of the synaptic environment occurring during small hemorrhagic stroke. The experimental data described here indicate that astrocyte remodeling is not a rare phenomenon that only happens in experimental conditions mimicking pathological states, but can also occur daily under physiological conditions in the hippocampus. These recurring, circadian changes in the relative proximity of astrocytes and spines occur in concert with changes in glutamate receptor activation in pyramidal neurons, which might be exacerbated by concurrent changes in the release of the NMDA receptor co-agonist D-Serine from astrocytes (Papouin et al., 2017). Together, these phenomena allow the brain to regularly sculpt the fundamental units of its neuronal circuits and provide a new mechanistic understanding of the molecular events that control the circadian modulation of synaptic plasticity and memory formation in the hippocampus.

We can only speculate on why the brain invests its energies in constantly turning up and down the strength of its synaptic connections. One possibility is that this may be a necessary step in a long-term investment plan, whereby tuning down synaptic efficacy during the D-phase may bring the hippocampus into a low energy-demanding state, to parse energy consumption over longer periods of time (Attwell and Laughlin, 2001). Because of these fluctuations, hippocampal networks may be able to switch between functioning modes that best process different types of information at specific time points during the day. Our data may provide a mechanistic basis for Marr's theory of the archicortex (Marr, 1971), in which the hippocampus alternates between times during which it stores information about patterns of neural activity representing events as they happen, and times during which this information is transferred to other regions of the brain, including the neocortex (Willshaw et al., 2015). Based on our experiments, for nocturnal animals like mice, the time to store information locally would be the L-phase, whereas the time to relay information to the neocortex would be the active D-phase.

LTP, melatonin and glucocorticoids

The first observation that LTP expression at hippocampal Schaffer collateral synapses varies at different times of the day dates back to 1983, when Harris and Teyler first showed that LTP at Schaffer collateral synapses in juvenile and adult rats was more robust in slices prepared during the L-phase (Harris and Teyler, 1983). Based on the fact that these results were obtained in reduced slice preparations, it was concluded that they did not depend on the activity of extra-hippocampal afferents but rather on the enduring effects of modulators that are lost very slowly from slice preparations, for example hormones.

Similar conclusions were later obtained in hamsters (Raghavan et al., 1999), highlighting the need to determine the underlying causes.

One of the first candidate molecules that was thought to mediate these effects was the hormone melatonin, mainly synthesized during the D-phase in the pineal gland from the precursor serotonin (Vanecek, 1998). In acute hippocampal slices, exogenously applied melatonin blocks LTP induction without altering low-frequency synaptic transmission (Collins and Davies, 1997; Wang et al., 2005). These effects are unlikely to be mediated by melatonin binding directly to melatonin receptors, because few receptors are expressed in the hippocampus. Given that melatonin has close structural similarity to various antagonists of the glycine-binding site of NMDA receptors (Huettner, 1989; Salituro et al., 1990; Salituro et al., 1992), it has been suggested that melatonin could reduce LTP by antagonizing NMDA receptors. This hypothesis has been tested and ultimately disputed by Collins and Davies (Collins and Davies, 1997). If melatonin does not have any known membrane receptor target, how does it exert its biological actions? Because of its hydrophobicity, melatonin released from the pineal gland into the bloodstream can easily pass through cell membranes. This allows melatonin to modulate a variety of intracellular molecular pathways and even bind to nuclear receptors (Carlberg and Wiesenberg, 1995; BenitezKing et al., 1996; Rafii-El-Idrissi et al., 1998; Benitez-King et al., 2001). Naturally, some of these interactions could have a deleterious effect on LTP. The problem is that many inbred strains of laboratory mice, like C57BL/6J, have no detectable levels of melatonin in the pineal gland due to two independent mutations in the genes encoding the biosynthetic enzymes for melatonin: N-acetylserotonin and hydroxyindole-o-methyltransferase (Ebihara et al., 1986; Kasahara et al., 2010; Peirson et al., 2018). It is therefore unlikely that our circadian effects on astrocyte morphology and AMPA EPSC summation are mediated by melatonin acting on molecular targets aside from MT1/2 receptors.

Other hormones known to be produced with circadian rhythmicity are adrenal corticosteroids, which act by activating glucocorticoid and mineralocorticoid receptors (Chung et al., 2011). High-affinity (Type I) mineralocorticoid receptors and low-affinity (Type II) glucocorticoid receptors are abundantly expressed in the hippocampus and both affect synaptic plasticity and memory formation (Kim and Yoon, 1998). Because of their different steady-state affinity, Type I receptors are fully occupied at low glucocorticoid plasma levels, whereas Type II receptors become fully occupied only with higher glucocorticoid plasma levels (Pavlides et al., 1995; Chung et al., 2011). Physiological increase in alertness and arousal during the D-phase of the circadian cycle can activate both types of receptors. Although the exclusive activation of Type I receptors promotes LTP, the concomitant activation of Type II receptors suppresses it (Pavlides et al., 1995). Consistent with these findings, our experiments show that the detected loss of LTP in the D-phase is associated with activation of both Type I and Type II receptors. To the best of our knowledge, the molecular and cellular mechanisms leading Type I-II receptor activation to loss of LTP had not been previously determined.

Generalizability and functional implications

Mice have evolved as nocturnal animals because they have fewer predators at night, making this the prime time to search for food. This nocturnal pattern of activity is still detected in mice kept in captivity. Although most animal facilities offer *ad libitum* access to food, caretakers are generally not around at night and therefore this remains the time of least perceived danger. In both nocturnal and diurnal species, the production of melatonin peaks during the D-phase, due to the fact that light inhibits its production through the activation of retino-hypothalamic afferent projections to the SCN. In contrast, the timing of glucocorticoid production coincides with the active phase, which is inverted between nocturnal and diurnal animals. This is because light exerts different effects on the light-sensitive neurons in the SCN of diurnal and nocturnal species. In diurnal species, light reduces the firing rate of photosensitive neurons.

By contrast, in nocturnal species, light increases the firing rate of these cells. Given that activation of the SCN inhibits the HPA axis through the release of vasopressin, light stimulates the release of corticosteroids in diurnal but not in nocturnal animals (Jiao et al., 1999; Smale et al., 2003). Therefore, to a first approximation, the production of corticoisteroids in humans and mice is locked to their activity phase (Dickmeis, 2009). Because in our experiments activation of corticosteroid receptors disrupts plasticity at Schaffer collateral synapses, it is tempting to speculate that synaptic plasticity might also be degraded in the human hippocampus through mechanisms similar to those described here but with opposite periodicity. However, since there are numerous molecular and behavioral differences and similarities between humans and mice, one needs to be cautious before jumping to the conclusion that L-phase of humans is analogous to the D-phase of a mouse. That said, our findings indicate that there are circadian changes in the molecular landscape of the hippocampus that enable this structure of the brain to switch to different functional modes. As a substantial reprogramming of oscillating transcripts occurs in temporal lobe epilepsy (Debski et al., 2017), our findings may have important implications to advance not only our understanding of circadian rhythmicity during physiological conditions but also to understand the pathogenesis and treatment of this and other chronic disease states.

Materials and Methods

Ethics statement

All experimental procedures were performed in accordance with protocols approved by the Institutional Animal Care and Use Committee at the State University of New York (SUNY) Albany and guidelines described in the National Institutes of Health's Guide for the Care and Use of Laboratory Animals.

Mice

Unless otherwise stated, all C57BL/6 mice were group housed and kept under a 12:12 hr L/D-cycles. The lights were turned on at Zeitgeber time 0 (ZT0), which in our animal facility was 7:00 AM. The fact that the ZT time sets the origin ot the 24 hour period to the beginning of the L-phase allows comparisons among studies independently of the actual clock-time settings of different animal facilities. Food and water were available *ad libitum* throughout the circadian cycle. Unless otherwise stated, all dissections for the L-phase data were performed at ZT3.5. All dissections for the D-phase data were performed at ZT15.5.

In vivo chronic temperature recordings

To record the mouse body temperature, we implanted programmable micro-transponders (Cat# IPTT300; BDMS) under the skin of the neck of P12 mice. We took temperature measures hourly from P14–21 using a wireless hand-held reader for IPTT micro-transponders (Cat# DAS-8007-IUS, BDMS). Data analysis was performed in IgorPro 6.37 (Wavemetrics, Lake Oswego, OR) using custom-made software (A.S.).

Fluorescent in situ hybridization of clock gene transcripts using RNAscope

We dissected the brain of P14-21 C57BL/6 mice at ZT3.5 or ZT15.5, removed the olfactory bulbs, cerebellum and temporal lobes and fixed it with 4% PFA/PBS overnight at 4°C. The brain was then cryo-protected in 30% sucrose PBS at 4°C for 48 hr and stored in PBS for no more than a week. To prepare slices for RNAscope, we separated the two hemispheres, embedded them in agar and prepared 40 µm thick slices using a vibrating blade microtome (VT1200S, Leica Microsystems, Buffalo Grove, IL). The slices were post-fixed in 4% PFA/PBS for 30 min at room temperature (RT) and mounted onto Superfrost plus microscope slides. Mounted slices were used for fluorescence in situ hybridization (FISH) using an

RNAscope multiplex fluorescent assay (Advanced Cell Diagnostics, Newark, CA) according to manufacturer instructions, using Mm-Per2-C1 and Mm-Arntl-C2 RNA probes and Opal 520 and Opal 570 dyes (Akoya Biosciences, Menlo Park, CA). DAPI Fluoromount G was used as the mounting medium (Cat# 0100-02; SouthernBiotech, Birmingham, AL). The presence of *Per2* and *Arntl* transcripts was assessed using a confocal microscope (Zeiss LSM710) equipped with a Plan-Apochromat 63X/1.4NA oil objective. Image size was set to 1024x1024 pixels and represented the average of 8 consecutive frames.

Acute slice preparation and electrophysiology recordings

Acute coronal slices of the mouse hippocampus were obtained from C57BL/6 mice of either sex (P14–21), deeply anesthetized with isoflurane and decapitated in accordance with SUNY Albany Animal Care and Use Committee guidelines. The brain was rapidly removed and placed in ice-cold slicing solution bubbled with 95% O_2/5% CO_2 containing the following (in mM): 119 NaCl, 2.5 KCl, 0.5 $CaCl_2$, 1.3 $MgSO_4 \cdot H_2O$, 4 $MgCl_2$, 26.2 $NaHCO_3$, 1 NaH_2PO_4, and 22 glucose, 320 mOsm, pH 7.4. The slices (250 µm thick) were prepared using a vibrating blade microtome (VT1200S; Leica Microsystems, Buffalo Grove, IL). Once prepared, the slices were stored in slicing solution in a submersion chamber at 36°C for 30 min and at RT for at least 30 min and up to 5 hr. Unless otherwise stated, the recording solution contained the following (in mM): 119 NaCl, 2.5 KCl, 2.5 $CaCl_2$, 1 $MgCl_2$, 26.2 $NaHCO_3$, and 1 NaH_2PO_4, 22 glucose, 300 mOsm, pH 7.4. We identified the hippocampus under bright field illumination using an upright fixed-stage microscope (BX51 WI; Olympus Corporation, Center Valley, PA). To record evoked currents, we delivered constant voltage stimuli (50–100 µs) to a bipolar stainless steel electrode (Cat# MX21AES(JD3); Frederick Haer Corporation, Bowdoin, ME) positioned in *stratum radiatum*, ~100 µm away from the recorded cell. Whole-cell, voltage-clamp patch-clamp recordings were made using patch pipettes containing (in mM): 120 $CsCH_3SO_3$, 10 EGTA, 20 HEPES, 2 MgATP, 0.2 NaGTP, 5 QX-314Br, 290 mOsm, pH 7.2. All recordings were obtained using a Multiclamp 700B amplifier (Molecular Devices, San Jose, CA) and filtered at 10 KHz, converted with an 18-bit 200 kHz A/D board (HEKA Instrument, Holliston, MA), digitized at 10 KHz, and analyzed offline with custom-made software (A.Sc.) written in IgorPro 6.37 (Wavemetrics, Lake Oswego, OR). Patch electrodes (#0010 glass; Harvard Apparatus, Holliston, MA) had tip resistances of 5 and 3 MΩ when patching neurons and astrocytes, respectively. Series resistance was not compensated (~20 MΩ for neurons, ~10 MΩ for astrocytes) but was continuously monitored and experiments were discarded if this changed by >20%. Tetrodotoxin (TTX), 2,3-Dioxo-6-nitro-1,2,3,4-tetrahydrobenzo[f]quinoxaline-7-sulfonamide disodium salt (NBQX) and D,L-2-Amino-5-phosphonopentanoic acid (APV) were purchased from Hello Bio (Princeton, NJ; Cat# HB1035, HB0443, HB0251, respectively). (3S)-3-[[3-[[4-(Trifluoromethyl)benzoyl]amino]phenyl]methoxy]-L-aspartic acid (TFB-TBOA) was purchased from Tocris (Minneapolis, MN; Cat# 2532). All other chemicals were purchased from MilliporeSigma (Burlington, MA). All recordings were performed at RT.

Biocytin filling and confocal imaging

Biocytin 0.2–0.4% (w/v) was added to the intracellular solution used to patch astrocytes and neurons. Each cell was patched and filled for at least 20 min. The slices were then fixed overnight at 4°C in 4% PFA/PBS, cryo-protected in 30% sucrose PBS, and incubated in 0.1% streptavidin-Alexa Fluor 488 conjugate and 0.1% Triton X-100 for 3 hr at RT. The slices were then mounted onto microscope slides using Fluoromount-G mounting medium (Cat# 0100-01; SouthernBiotech, Birmingham, AL). Confocal images were acquired using a Zeiss LSM710 inverted microscope equipped with 488 nm Ar laser. All images were acquired as z-stacks using a 40X/1.4 NA oil-immersion objective. To visualize full cells, we stitched together z-stacks (1024x1024 pixels) collected by averaging four frames for each focal plane (1 µm z-step). The image analysis to measure the astrocyte coverage area was performed using Fiji (https://fiji.sc/). Briefly, we generated a maximum intensity projection of each image stack and manually

traced the contour of the outer boundaries of the area of the neuropil covered by each astrocyte. Confocal images that contained more than one filled astrocyte were discarded from the analysis, because they introduced inaccuracies in the derived contours. The polar plots were obtained by centering the soma of each astrocyte at the center of a polar plot. The main primary branch of each astrocyte was oriented along the 270° angle. Average coverage traces were obtained using IgorPro (Wavemetrics, Lake Oswego, OR).

Protein-retention expansion microscopy and two-photon imaging

All experiments were performed according to the proExM protocol described by (Tillberg et al., 2016). Briefly, to measure the expansion factor (**Fig. 10**) we fixed hippocampal slices with 4% PFA/PBS overnight at 4°C, cryoprotected them in 30% sucrose PBS and stored them in PBS. The day before starting the proExM protocol, we incubated them with DAPI Fluoromount G overnight at 4°C (Cat# 0100-20; SouthernBiotech, Birmingham, AL). Slices containing biocytin filled astrocytes were fixed, cryo-protected, stored in PBS and labelled with streptavidin-Alexa Fluor 488 as described in the previous section. In both cases, each slice was then incubated with 200 µl of anchoring solution overnight at RT. The following day, the slices were gelled and digested with Proteinase K overnight at RT. Subsequently, they were expanded using three consecutive incubations with distilled water for 15 min each. Slices stained with DAPI were imaged as they expanded during each incubation period, using a 2X/0.06 NA air objective on an EVOS FL Cell Imaging System equipped with DAPI filter set (λ_{ex}: 357/44 nm, λ_{em}: 447/60 nm; ThermoFisher Scientific, Waltham, MA). Images were collected at 0.1 fps and manually traced to measure slice perimeter and surface area using IMOD (https://bio3d.colorado.edu/imod/). The expanded gels containing biocytin-filled astrocytes were then covered with 2% agarose and submerged in distilled water before being imaged with a custom-made two-photon laser-scanning microscope. The two-photon laser scanning system (Scientifica, Clarksburg, NJ) was powered by a Ti:sapphire pulsed laser (Coherent, Santa Clara, CA) tuned to 760 nm and connected to an upright microscope with a 60X/1.0 NA objective (Olympus Corporation, Center Valley, PA). The green fluorescent signal was separated from the red using a 565 nm dichroic mirror and filtered using FITC filter sets (Olympus Corporation, Center Valley, PA). We averaged eight frames for each optical section (512×512 pixels) and collected z-stacks for a total distance of ~200 µm (in 1.2 µm steps). The composition of the anchoring, gelling and digestion solution is reported below.

Anchoring solution (200 µl/slice)

Acryloyl X, SE	Cat# A20770	Life Technologies	0.1 mg/ml
DMSO	Cat# 472301	Millipore Sigma	2 µl
PBS	Cat# P4417	Millipore Sigma	198 µl

Monomer solution (188 µl/slice)

Sodium acrylate	Cat# 408220	Millipore Sigma	86 mg/ml
Acrylamide	Cat# A9099	Millipore Sigma	25 mg/ml
N,N'-methylenebisacrylamide	Cat# M7279	Millipore Sigma	1.5 mg/ml
NaCl	Cat# 215700	BeanTwon Chemical	117 mg/ml
PBS 10X	Cat# P4417	Millipore Sigma	18.8 µl (1:10)
Distilled water			169.2 µl

Gelling solution (200 µl/slice)

Monomer solution			188 µl
4-hydroxy-TEMPO	Cat# 176141	Millipore Sigma	4 µl (0.01%)
TEMED	Cat# T9281	Millipore Sigma	4 µl (0.2% w/w)
APS	Cat# A3678	Millipore Sigma	4 µl (0.2% w/w)

Digestion solution (1 ml/slice)

Tris pH 8.0	Cat# AM9855G	Ambion	50 mM
EDTA	Cat# 03690	Fluka Analytical	1 mM
Triton X-100	Cat# X100	Millipore Sigma	0.5% v/v
Guanidine hydrochloride	Cat# G3272	Millipore Sigma	0.8 M
Proteinase K	Cat# P6556	Millipore Sigma	8 U/ml

Western blot

Western blot experiments were performed on protein extracts from the hippocampus of mice of either sex aged P14–21, sacrificed at ZT3.5 or ZT15.5. Membrane proteins were extracted using the Mem-PER Plus Membrane Protein Extraction Kit (Cat# 89842; ThermoFisher Scientific, Waltham, MA) according to the manufacturer's instructions using a mixture of protease and phosphatase inhibitors (10 µl/ml, Cat# 78441; ThermoFisher Scientific, Waltham, MA). The total membrane protein concentration was determined by spectrophotometry. Equal amounts of protein (100 µg) from each sample were resolved on 10 or 12% acrylamide gels. The proteins were transferred to PVDF membranes (Cat# P2563; MilliporeSigma, Burlington, MA) using a semidry blotting approach. The membranes were blocked with 5% nonfat milk in TBST pH 7.6, and probed with primary antibodies overnight at 4°C in 5% BSA in TBST, pH 7.6. Secondary antibody incubation was performed for 1–2 hr at RT in 5% nonfat milk in TBST, pH 7.6. Pre-adsorption experiments were performed using the control antigen provided by the primary antibody supplier according to the manufacturer's instructions (1 µg/µg antibody). Membranes were probed with either rabbit anti-GLAST (1:1,000), anti-GLT-1 (1:1,000) or β-actin antibodies (1:1,000). Biotinylated horse anti-rabbit antibody was used as the secondary antibody for all blots (1:1,000 for GLAST and GLT-1, 1:5,000 for β-actin). We amplified the immuno-labeling reactions using the Vectastain ABC kit (1:2,000 for GLAST and GLT-1; 1:5,000 for β-actin) and the Clarity Western ECL system served as the substrate for the peroxidase enzyme (Cat# 1705060, Bio-Rad, Hercules, CA). For semi-quantitative analysis, protein band intensities were collected as 16-bit images using a digital chemiluminescence imaging system (c300, Azure Biosystems, Dublin, CA) at different exposure times (0.5–200 s). Each image was converted to an 8-bit image for image analysis using Fiji software (https://fiji.sc/). Only images collected at exposure times that did not lead to pixel saturation were included in the analysis. The intensity of each band was calculated as the mean gray value in a region of interest (ROI) surrounding each band in 3 images collected at different exposure times. All GLAST and GLT-1 band intensities were normalized to the band intensity of β-actin in the same lane. Only images collected at exposure times that did not lead to pixel saturation were used to quantify band intensities.

A list of antibodies and reagents, with their RRID, is reported below:

RRID: AB_10695722	rabbit anti GLAST	Cell Signaling Technology, Danvers, MA
RRID: AB_2190743	rabbit anti GLT-1	Cell Signaling Technology, Danvers, MA
RRID: AB_2223172	rabbit anti β-actin	Cell Signaling Technology, Danvers, MA
RRID: AB_2336201	biotinylated horse anti-rabbit	Vector Laboratories, Burlingame, CA
RRID: AB_2336819	Vectastain ABC kit	Vector Laboratories, Burlingame, CA

Electron microscopy and axial STEM tomography

Acute hippocampal slices processed for electron microscopy analysis were prepared as described for the electrophysiology experiments, from P17 mice. Slices were microwave-fixed for 13 s in 6% glutaraldehyde, 2% PFA, 2 mM $CaCl_2$ in 0.1 N sodium cacodylate buffer and stored overnight at 4°C. After three washes in 0.1 N cacodylate buffer, we cut samples from the middle part of CA1 *stratum radiatum*, ∼100 µm away from the pyramidal cell layer. These samples were treated with 1% osmium tetroxide for 1 hr on ice, en bloc mordanted with 0.25% uranyl acetate at 4°C overnight, washed and dehydrated with

a graded series of ethanol, and embedded in epoxy resins. Thin sections (70–90 nm) were counterstained with lead citrate and uranyl acetate and examined on a JEOL 1200 EX transmission electron microscope. Images were collected with a CCD digital camera system (XR-100, AMT, Woburn, MA). To visualize the arrangement of pre-synaptic terminals, post-synaptic terminals, and astrocytic processes, thick sections (∼1 µm) were cut from regions of CA1 *stratum radiatum* and electron tomograms were collected in a 300 kV electron microscope operated in the scanning transmission electron microscopy (STEM) mode, as described previously (Hohmann-Marriott et al., 2009; Sousa et al., 2011). A sample thickness of 1 µm – enabled by axial STEM tomography – provided sufficient sample depth to visualize features of interest in their entirety, such as synapses. In contrast to standard TEM tomography, conventional TEM tomography is limited to a specimen thickness of ∼400 nm and cannot be applied to such thick sections because the transmitted electrons undergo multiple inelastic scattering processes, resulting in images that are blurred by chromatic aberration of the objective lens. Axial STEM tomography is not affected by chromatic aberration because the objective lens that forms the electron probe is in front of the specimen. Dual-axis tilt series of selected sections were recorded using an FEI Tecnai TF30 TEM/STEM operating at 300 kV (1.5° tilt increment, tilt range from 55° to −55°, pixel size = 5.6 nm). Image registration, tomogram generation, tracing, surface area and volume measures were performed using IMOD 4.7 (http://bio3d.colorado.edu/imod/). In the tomograms, we identified astrocytic processes based on their lack of synaptic vesicles and post-synaptic densities and because they did not give rise to pre- or post-synaptic terminals. Orthoslices through the STEM tomograms showed that astrocytic processes contained glycogen granules, intermediate filament bundles and a more electron-lucent cytoplasm with respect to that of neurons. The astrocytic processes were traced for the entire thickness of the reconstructed volume (1–1.5 µm). We reconstructed all astrocytic processes and all PSDs in each block. The reconstructed volumes were converted into object files and imported into the open-source software Blender 2.76 (https://www.blender.org/). Astrocyte-PSD distance was measured in Blender using custom-made analysis software written in Python (Sweeney et al., 2017).

Tomographic holographic 3D microscopy

The measures of the cell membrane to cytoplasm ratio were obtained from acute hippocampal slices, prepared as described in the electrophysiology section of the methods, from animals aged P14–21 at ZT3.5 (L-phase) or ZT15.5 (D-phase). We used slices prepared at ZT3.5 for our osmolality test. Briefly, we prepared different batches of the slice recording solution, with different concentrations of NaCl (95, 107, 119, 131, 143 mM). We measured the osmolality of these solutions using a vapor pressure osmometer (Wescor 5600, Wescor, Logan, UT). Each slice was stored in one of these solutions for 1 hr, then it was fixed overnight with 4% PFA/PBS and cryo-protected in 30% sucrose PBS. The slices were then re-sectioned at 40 µm thickness using a vibrating blade microtome (VT1200S, Leica Microsystems, Buffalo Grove, IL) and mounted on a microscope slide using Fluoromount-G mounting medium (Cat# 0100-01; SouthernBiotech, Birmingham, AL). The slices were then imaged using the 3D Cell Explorer holographic tomographic 3D microscope (Nanolive, Ecublens, Switzerland) equipped with a 60X objective (NA=0.8), a class I laser source at λ=520 nm with a power output of 0.1 mW (sample exposure = 0.2 mW/mm^2), and a USB 3.0 CMOS Sony IMX174 sensor providing 1024×1024 pixels at 165 fps (Cotte et al., 2013). The output data were acquired as image stacks of 512×512×96 voxels (0.186×0.186×0.372 µm) with a rate of tomogram acquisition of 0.5 s^{-1}. This label-free non-phototoxic type of microscopy measures the refractive index (RI) in 3D samples, and allows users to visualize it using different levels of tolerance referred to as the refractive index gradient (IG). The acquired images were processed using Software for Tomographic Exploration of living cElls (STEVE) and Fiji (https://fiji.sc/). By using STEVE, we digitally stained the cells' membrane (RI = 1.327–1.333; IG = 0.015–0.070) and cytoplasm (RI = 1.329–1.330; IG = 0.007–0.021). The RI and IG settings were varied across slices, but remained constant for our measures in the pyramidal cell layer and *stratum radiatum* of hippocampal area CA1. By using Fiji, we calculated the number of digitally

stained pixels in three ROIs (200×100×40 pixels) positioned in the CA1 pyramidal cell layer and *stratum radiatum* of each slice. The center of the ROIs along the z-axis was positioned half way through the original z-stack acquired using the 3D Cell Explorer.

Computational Modelling

3D z-stacks of biocytin filled CA1 pyramidal neurons were acquired using a Zeiss LSM710 confocal microscope and saved as czi files. The czi files were imported into Fiji (https://fiji.sc/) using the Simple Neurite tracer v3.1.3 plugin (http://imagej.net/Simple_Neurite_Tracer), first developed by (Longair et al., 2011). The radius of the soma was calculated as the radius of an equivalent circle with the same area of the soma obtained from the maximum intensity projection of the confocal z-stacks. When using this plugin, we first picked the location of the center of the soma and then manually traced the 3D trajectory of different neuronal processes. Each process was tagged as axon, basal or dendritic branch so that they could be assigned different conductances. The tracings were converted into .swc and .asc files to be imported in the NEURON simulation environment v7.6 (Hines and Carnevale, 1997). All model and simulation files will be uploaded to the ModelDB database (https://senselab.med.yale.edu/modeldb/, acc. n. 257027). Also, the morphology will be uploaded to the neuromorpho.org database (www.neuromorpho.org), and an interactive "live paper" page will be setup in the Brain Simulation Platform of the Human Brain Project (https://www.humanbrainproject.eu/en/brain-simulation/live-papers/). To implement a CA1 pyramidal neuron model, we used the 3D accurate morphology reconstructed within this work (**Fig.5D**) equipped with the typical somatodendritic distribution of channels observed in rodents hippocampal CA1 pyramidal neurons (Migliore and Shepherd, 2002). The channel kinetics were identical to those used in (Migliore et al., 2018) (ModelDB acc.n. 244688). The AMPA synapse kinetic model was from (Tsodyks et al., 1998) (ModelDB acc.n. 3815), with *tau_1*= 4.5 ms, a peak conductance of 0.2 nS, and a *tau_rec* of 10 ms or 30 ms to model light and dark condition, respectively. The NMDA kinetics was taken from (Gasparini et al., 2004) (ModelDB acc.n. 44050) with the reverse (unbinding) rate β=0.005 ms^{-1} and a peak conductance of 0.7 nS or 0.55 nS to reproduce light and dark conditions, respectively. To mimic the train of synaptic activations caused by an extracellular electrical pulses we added 20 synapses randomly distributed in the apical dendrites between 50 and 300 μm from the soma, synchronously activated every 10 ms.

Data analysis

Electrophysiological recordings were analyzed within the Igor Pro environment using custom made software (A.S.). Synaptically activated transporter currents (STCs) were isolated as described previously (Diamond, 2005; Scimemi et al., 2009; Sweeney et al., 2017). Briefly, single and pairs of stimuli, 100 ms apart, were delivered every 10 s. We averaged 10 single and 10 STC pairs and subtracted single from paired STCs to isolate the current evoked by the second pulse. The single STC was then shifted in time by 100 ms (the inter-pulse interval), so that its onset matched the onset of the second STC. The current obtained by subtracting the time-shifted single STC from the paired STCs represented the facilitated portion of the STC (fSTC). This analytical strategy allowed us to get rid of the sustained potassium current that is superimposed on the STC but does not facilitate with repeated stimulation. In the unlikely event that a component of the sustained potassium current was still present after this subtraction, we removed it by subtracting a mono-exponential function with an onset time of 4 ms and an amplitude that was scaled to match the amplitude of the remaining potassium current (Scimemi et al., 2009). We used the fSTCs in control conditions and in the presence of a sub-saturating concentration of TFB-TBOA (1 μM) to calculate the time course of glutamate clearance by performing a deconvolution analysis of the STCs (Diamond, 2005; Scimemi et al., 2009; Sweeney et al., 2017). *First,* the STCs recorded under control conditions and in TFB-TBOA (1 μM) were binomially smoothed and fitted with the following equation (Nielsen et al., 2004):

$$F(t) = A_1\left(1 - e^{\frac{t_0 - t}{\tau_{rise}}}\right)^n \left(e^{\frac{t_0 - t}{\tau_{fast}}} + A_2 e^{\frac{t_0 - t}{\tau_{slow}}}\right)$$

Second, we approximated glutamate clearance in TFB-TBOA (1 µM) with an instantaneously rising function decaying mono-exponentially, with the same time course of the STC. *Third,* we deconvolved this approximated glutamate clearance from the STC recorded in low TFB-TBOA to obtain the filter. *Fourth,* we deconvolved the filter from the STC recorded in control conditions to obtain the glutamate clearance waveform in control conditions.

Miniature events were detected using an optimally scaled template (Clements and Bekkers, 1997) adapted for Igor Pro (A.S.). Paired-pulse ratio (PPR) of EPSCs was calculated by subtracting single from paired EPSCs averaged across 20 traces, after first peak normalization. When delivering trains of stimuli, we interleaved single pulses with trains of four and five pulses. The 5th EPSC was isolated by subtracting the average response to four pulses from the average response to five pulses.

Image preprocessing for Sholl analysis

The Sholl analysis was performed on adaptively thresholded maximum intensity projections of filtered confocal z--stacks. Each plane of the z-stack was first filtered with a coherence-enhancing diffusion filter (Weickert and Scharr, 2002), and then we filtered the maximal projection intensity image as described below. Astrocytic processes are generally thin and elongated. To take advantage of this property, we used steerable oriented filters and stored in each pixel the maximal response to different filter sets. Any region near a round bright spot is "oriented" towards it, meaning that the maximal response is obtained with respect to the filter with similar orientation. We used a round isotropic Gaussian filter to find local intensity maxima and oriented filters to highlight the thin elongated structures. To suppress the algorithm from detecting false-positive filamentous structures in dark and noisy regions of interest we performed a randomization-based regularization consisting of many iterations in which we disturbed the input image with noise and then thresholded the responses. By averaging the results obtained over multiple iterations, we obtained an estimate of the probability that each pixel has an oriented structure brighter than its surroundings. The final mask is the product of the isotropic and anisotropic filter responses.

Image analysis of complexity and entropy

The complexity-entropy analysis allows quantification of the spatial properties of representative images with respect to their balance between randomness and structural order, triviality and complexity as previously described (Brazhe, 2018). In mathematical terms, this is described as location in the complexity-entropy plane or their distribution along a complexity-entropy spectrum. Highly ordered structures (e.g., a regular grating) have near-zero entropy and near-zero complexity. In contrast, completely disordered structures (e.g., independent and identically distributed Gaussian samples) have maximal entropy and small statistical complexity. Intermediate values of entropy are associated with higher values of complexity if the underlying pattern contains features with preferred orientation. For example, signals generated by systems with deterministic chaos result in a complexity-entropy spectrum with near-0.5 peak complexity and near-0.7 entropy (Lamberti et al., 2004; Rosso et al., 2007). The implementation code is available at DOI:10.5281/zenodo.1217636. Briefly, complexity and entropy measures can be based on a feature distribution of the analyzed patterns, which can be compared to equiprobable or singular feature cases. Accordingly, the relative entropy (H) was defined as the Shannon entropy:

$$H[P] \coloneqq \frac{S[P]}{S_{max}} = (-\sum_{i=1}^{N} P_i \log_2 P_i) / \log_2 N$$

normalized by the entropy of an equally probable distribution (S_{max}), thus giving values in the range [0 … 1]. Here N is the number of features analyzed. The complexity measures were based on the notion of disequilibrium (Lamberti et al., 2004) and defined in terms of normalized Jensen-Shannon divergence from an equally probable distribution (Rosso et al., 2007):

$$C[P] \coloneqq H[P]J[P, P_e]/J_{max}$$

In this expression, $J[P,P_e]$ is Jensen-Shannon divergence of some distribution P from an equally probable distribution P_e:

$$J[P, P_e] = S\left[\frac{P + P_e}{2}\right] - \frac{1}{2}(S[P] + S[P_e])$$

and J_{max} is obtained when the probability of just one feature is equal to 1, while the probability of all other features is zero. The defined probability-based definitions of entropy and complexity require building descriptive probability-like measures for spatial patterns, preferably allowing for multiscale resolution and local analysis. A spatial pattern can be described in terms of local edge orientations and scales, which can be achieved by discrete shearlet transform, which is analogous to wavelet transform with added orientation information. We treated normalized power of shearlet coefficients as probability densities of given spatial feature orientation and scale at a given location. Complexity and entropy calculations were only performed in regions containing non-zero pixels, while other areas were masked out.

Statistical analysis

Data are presented as mean±SEM unless otherwise stated. All experiments were performed on multiple mice of either sex. Statistical significance was determined by Student's paired or unpaired t test or ANOVA, as appropriate (IgorPro 6.37). Differences were considered significant at $p<0.05$ (*$p<0.05$; **$p<0.01$; ***$p<0.001$).

Acknowledgements

We would like to thank Drs. Pablo Valdes and Ed Boyden for support with the proExM protocol and Drs. Juan Burrone, Christophe Bernard and Damian Zuloaga for valuable discussions.

Competing Interests

None to declare.

Author Contributions

Conceptualization: A.Sc.
Methodology: A.B., A.Sc.
Formal Analysis: J.P.M., L.Y.D., N.A., J.J.W., S.Z., S.S., A.A.S, R.M., A.Sc.
Investigation: J.P.M., M.A.P., L.Y.D., G.C.T., N.A., R.M., A.Sc.
Resources: R.D.L., A.K., A.Se., M.M., A.Sc.

Writing – Original Draft Preparation: A.Sc.
Writing – Review & Editing: All authors
Visualization: A.Sc.
Supervision: A.Sc.
Project Administration: A.Sc.

Funding Acquisition: This work was supported by the Presidential Award for Undergraduate Research and Initiative for Women Award to N.A.; RFBR COMFI (Grant Number 17-00-00412K) for joint research to A.Se. (Grant Number 17-00-00409) and A.B. (Grant Number 17-00-00407); NIH/National Institute of Biomedical Imaging and Bioengineering Intramural Research Program (Grant Number ZIAEB000046) to R.D.L.; NIH/National Institute on Drug Abuse (Grant Number R01DA04741001) to A.K.; EU H2020 program (Grant Number 785907, HBP SGA2) to M.M. and R.M.; NIH/National Institute of Neurological Disorders and Stroke (Grant Number R03NS102822), SUNY Albany and SUNY Albany Research Foundation to A.Sc.

Figure Legends

Figure 1. Circadian rhythmicity is present in juvenile mice and is associated with changes in hippocampal plasticity. (A) Average hourly body temperature values measured using subcutaneous transponders on P14-21 mice. The white and blue shaded areas in the graph represent the L-phase (ZT0-12) and D-phase (ZT12-24), respectively. The white and blue dots represent the position of the maximum and minimum temperature during each circadian cycle, respectively. The thin orange line and yellow shaded areas represent the mean±SEM. The thick orange line represents the smoothed mean, obtained using a boxcar smoothing algorithm with 10 repetitions and a 5-point boxcar width. The grey and blue curves at the top and bottom of the figure represent a multi-peak fit of the data collected from each mouse, to determine the position of the maximum (top) and minimum body temperature for each mouse (bottom). Regularly spaced peaks for maximum and minimum body temperature occur with circadian and alternate rhythmicity in P14-21 mice. **(B)** As in (A), on data obtained after subtraction of the mean body temperature of each mouse, obtained by averaging the measurements over the entire duration of the experiment. **(C)** Schematic representation of a mid-sagittal section of the mouse brain. The light blue square represents the location of the SCN region from which we collected confocal images. The green and red puncta represent the RNAscope signal for transcripts of clock genes *Arntl* (green) and *Per2* (red) in slices prepared at ZT3.5 (light) and ZT15.5 (dark). The bar charts on the right provide a summary of the *Arntl* and *Per2* puncta density. **(D)** As in (C), for the pyramidal cell layer of hippocampal area CA1. **(E)** As in (C), for measures obtained in *stratum radiatum*. **(F)** *Top left,* time course of baseline-subtracted ratio between the field EPSC slope and the fiber volley amplitude in slices prepared at ZT3.5 (light, black) and ZT15.5 (dark, blue). The induction protocol consisted of 10 bursts at 10 Hz (100 Hz and 0.05 s each). *Bottom left,* time course of baseline-subtracted ratio between the field EPSC slope and the fiber volley amplitude in slices prepared at ZT3.5 (subjective light, green) from mice kept under constant darkness. *Right,* average responses recorded in each condition 5 min before and 30 min after TBS. **(G)** Summarized effect of TBS in light, dark and constant darkness.

Figure 2. Blocking corticosteroid receptors rescues LTP in the dark phase. (A) *Left,* time course of baseline-subtracted ratio between the field EPSC slope and the fiber volley amplitude in slices prepared at ZT3.5 (light), in the presence of the NR3C1 mineralocorticoid receptor antagonist spironolactone (10 µM). *Middle,* average responses recorded 5 min before and 30 min after TBS. *Right,* summarized effect showing that LTP expression was not affected by spironolactone. **(B)** As in (A), in the presence of the NR3C2 glucocorticoid receptor antagonist mifepristone (1 µM). **(C)** As in (A), in the presence of the

melatonin receptor antagonist luzindole (50 µM). **(D)** *Left,* time course of baseline-subtracted ratio between the field EPSC slope and the fiber volley amplitude in slices prepared at ZT15.5 (dark), in the presence of the NR3C1 mineralocorticoid receptor antagonist spironolactone (10 µM). *Middle,* average responses recorded 5 min before and 30 min after TBS. *Right,* summarized effect showing that LTP expression was rescued by spironolactone in slices prepared during the dark phase. **(E)** As in (D), in the presence of the NR3C2 glucocorticoid receptor antagonist mifepristone (1 µM). **(F)** As in (D), in the presence of the melatonin receptor antagonist luzindole (50 µM).

Figure 3. NMDA receptor activation in CA1 pyramidal cells is reduced during the dark phase. (A) Example of single and paired AMPA and NMDA EPSCs, recorded at a holding potential of -65 mV and 40 mV, respectively. Each trace represents the average of 20 stimulations, delivered with a 10 s inter-stimulus interval. **(B)** Summary graph of the paired-pulse ratio (PPR) for AMPA and NMDA EPSCs. **(C)** Peak-normalized AMPA EPSCs recorded during the L/D-phases. **(D)** Summary of the amplitude and kinetics analysis of AMPA EPSCs. No significant difference in the amplitude, rise and half-decay time was detected during the L/D-phases. **(E)** Peak-normalized NMDA EPSCs recorded during the L/D-phases. **(F)** Summary of the amplitude and kinetics analysis of NMDA EPSCs. The amplitude of NMDA EPSCs was smaller during the D-phase. **(G)** Average AMPA and NMDA EPSCs, normalized by the peak of the AMPA current in each cell. **(H)** The NMDA/AMPA ratio, scaled by their corresponding driving force, was reduced in the D-phase. **(I)** Average electrically-evoked AMPA and NMDA EPSCs recorded from CA1 pyramidal cells in the presence of RuBi-glutamate (100 µM). **(J)** The amplitude of electrically-evoked NMDA, not AMPA EPSCs, was smaller in slices prepared at ZT15.5. **(K)** Average flash-evoked AMPA and NMDA EPSCs recorded from CA1 pyramidal cells in response to RuBi-glutamate uncaging (100 µM). **(L)** The amplitude of uncaging-evoked NMDA, not AMPA EPSCs, was smaller in slices prepared at ZT15.5.

Figure 4. CA1 pyramidal cells have similar spine density during the light and dark phases. (A) Biocytin-filled dendritic branches of CA1 pyramidal cells in slices prepared at ZT3.5 (light) and ZT15.5 (dark). The confocal images were acquired as confocal z-stacks using a 63X/1.4 NA oil objective. They were subsequently converted into maximum intensity projections and processed with a Canny-Deriche filtering for edge detection using Fiji. **(B)** Summary of spine linear density, showing no significant difference between samples fixed during the light and dark phase.

Figure 5. Temporal summation of AMPA EPSCs is reduced during the D-phase. (A) *Left,* train of AMPA EPSCs recorded in voltage clamp mode while holding pyramidal cells at a holding potential of -65 mV. Each train stimulation was composed of five pulses, with an inter-pulse interval of 10 ms. The AMPA EPSC summation was reduced in the D-phase. *Right,* as the panels described on the left hand side, for NMDA EPSCs recorded at a holding potential of 40 mV. NMDA EPSC summation is similar during the L/D-phases. **(B)** *Left,* ChanneLab simulations of AMPA EPSCs evoked by five consecutive glutamate release events, with a peak glutamate concentration of 1 mM and an inter-event interval of 10 ms. The kinetic scheme of AMPA receptors was taken from (Jonas et al., 1993). The decay time of each glutamate transient (τ) was color-coded according to the scheme on the left hand side of the figure. Longer glutamate transients lead to reduced AMPA EPSC summation. *Right,* as the left panels, for NMDA EPSCs. The kinetic scheme for NMDA receptor activation was taken from (Lester and Jahr, 1992). Longer glutamate transients did not lead to significant changes in NMDA EPSC summation. **(C)** Results of NEURON multi-compartmental model. *Left,* the traces represent somatic AMPA EPSP evoked by activating a cohort of 100 synapses randomly distributed through the dendritic tree of CA1 pyramidal cells. Changes in the recovery rate of the AMPA receptors, mimicking those induced by prolonged glutamate clearance, reduced the temporal summation of consecutive EPSPs. The second panel of this figure shows the evoked EPSPs on an expanded time scale. The right panels show the somatic change in potential evoked by activating the same cohort

of excitatory synapses that in this case only contained NMDA receptors. To mimic the experimental results obtained during the D-phase, we reduced the NMDA conductance at each synaptic contact. **(D)** Morphology of the biocytin-filled CA1 pyramidal cell neuron used to run the NEURON simulations. The summary graphs provide an overview of the normalized cumulative AMPA and NMDA EPSP amplitude recorded in modeling conditions that mimic experimental data collected during the L/D-phases.

Figure 6. Glutamate clearance from the extracellular space is slower during the D-phase. (A) Example of whole-cell recordings from astrocytes obtained in voltage-clamp mode, in the presence of the $GABA_A$ and AMPA receptor antagonists picrotoxin (100 µM) and NBQX (10 µM). Extracellular stimuli to Schaffer collaterals evoked a brief fiber volley (FV) followed by a fast-decaying STC and a slow-decaying potassium current (I_K). **(B)** The amplitude of the sustained potassium current was proportional to the amplitude of the evoked fiber volley and this relationship remained unaltered across the L/D-phases. **(C)** Summary graph of the amplitude and kinetics of STCs evoked in slices prepared during the L/D-phases. We used extracellular stimulus strengths that evoked STCs of similar amplitude during the L/D-phases. The evoked STCs displayed similar 20-80% rise time but their half-decay time (t_{50}) and centroid (<*t*>) were prolonged during the D-phase. **(D)** The facilitated portion of the STC (fSTC) was isolated by subtracting single from paired STCs and was used to estimate the time course of glutamate clearance from astrocytes (Scimemi and Diamond, 2013). The high-affinity, broad-spectrum glutamate transporter antagonist TFB-TBOA (1 µM) reduced the fSTC amplitude significantly and to a similar extent during the L/D-phases. The fSTC rise, half-decay time and centroid were larger in the presence of TFB-TBOA. The similar effects of TFB-TBOA on slices prepared during the L/D-phases was an important pre-requisite for the deconvolution analysis of fSTCs. **(E)** Average astrocyte glutamate clearance waveforms during the L/D-phases (mean±SEM). **(F)** Summary graph showing that glutamate clearance by astrocytes is slower during the D-phase.

Figure 7. The passive membrane properties of astrocytes and neurons do not change during the L/D-phases. (A) Example of voltage step protocol and current responses recorded from astrocytes patched in *stratum radiatum* of acute hippocampal slices prepared during the L/D-phases. Each voltage step was 100 ms long. The holding membrane potential (-80 mV) was stepped from -100 mV up to 40 mV, in 20 mV voltage steps. Each current response represents the average of 20 responses from one astrocyte. A 10 ms, 5 mV hyperpolarizing voltage step was used to monitor changes in the series resistance of our recordings. Any recording in which the series resistance changed more than 20% compared to its initial value was discarded from the analysis. **(B)** I/V relationship derived from the experiment described in (A), during the L/D-phases. Thick lines and shaded areas represent mean±SEM. **(C)** Close-up view on the voltage step protocol and current responses. The decaying phase of the current responses provided information on the astrocyte capacitance. **(D)** *Left,* the astrocyte input resistance (R_{in}) was similar during the L-phase (white bar and grey dots) and D-phase (blue bar and light blue dots). *Right,* the astrocyte membrane capacitance (C_m) was similar during the L/D-phases. **(E)** *Left,* CA1 pyramidal cells had higher input resistance and membrane capacitance compared to astrocytes. The input resistance was similar during the L/D-phases. *Right,* the membrane capacitance was also similar during the L/D-phases. **(F)** *Left,* the resting membrane potential of astrocytes did not change significantly in the L/D-phases. *Right,* the number of dye-coupled astrocytes was measured in confocal images of biocytin-filled, streptavidin-AF488-labeled cells, and was similar during the L/D-phases.

Figure 8. Astrocytic glutamate transporter expression is not altered during the L/D-phases. (A) Western blot analysis of hippocampal GLAST expression. The two upper bands correspond to GLAST monomers and dimers. **(B)** Quantification of GLAST band intensity, normalized to the corresponding intensity of β-actin, in the L/D-phases. **(C)** Quantification of GLAST band intensity normalized by the normalized band intensity in the L-phase. **(D)** Western blot analysis of hippocampal GLT1 expression. The

two upper bands correspond to GLT1 monomers and dimers. **(E)** Quantification of GLT1 band intensity, normalized to β-actin, in the L/D-phases. **(F)** Quantification of GLT1 band intensity normalized to the β-actin-normalized measures obtained in the L-phase.

Figure 9. No overt phenomenon of cell swelling or shrinkage occurs the hippocampal neuropil during the L/D-phases. (A) Example images of hippocampal area CA1, collected using holotomography in slices stored in extracellular solutions of different osmolality. Each image was digitally stained using refractive index value (RI) and gradient (IG) combinations that allowed labeling cell membranes (yellow) and cell cytoplasm (magenta). Cell shrinkage was detected at higher extracellular osmolality. **(B)** The scatter plots show the specific combinations of RI value and gradient used to label cell membranes (left) and cytoplasm (right) across slices. **(C)** Scatter plot of the membrane to cytoplasm (M/C) ratio measured in the pyramidal cell layer of hippocampal area CA1 at different osmolality values. Black lines and grey shaded areas represent the linear fit of the data and 95% confidence interval. The r-value in the top left corner of the graph represents the Pearson's correlation coefficient. **(D)** As in (C), for measures obtained in *stratum radiatum*. **(E)** Example images collected from slices prepared during the L/D-phases. **(F)** Scatter plot of RI value and gradient combinations use to label cell membranes (left, yellow) and cell cytoplasm (right, magenta) in slices prepared during the L/D-phases. **(G)** Summary graph of M/C ratio measures, showing similar M/C ratio values during the L/D-phases.

Figure 10. proExM provides a similar expansion of hippocampal slices prepared during the L/D-phases. (A) *Left,* fluorescence microscopy image of a hippocampal slice labelled with DAPI. The high cell density, bright area is the dentate gyrus. *Middle,* fluorescence microscopy image of the same hippocampal slice after three consecutive, 15 min long rounds of expansion. *Right,* overlaid image of the expanded dentate gyrus scaled down to the size of the hippocampal slice before expansion. This comparison shows that proExM generates an isotropic expansion of hippocampal slices. **(B)** Time course of hippocampal slice area increase during the proExM protocol, in slices prepared during the L-phase. **(C)** As in (B), in slices prepared during the D-phase. **(D)** Quantification of the proExM-induced surface area increase in hippocampal slices. **(E)** Time course of hippocampal slice perimeter increase during the proExM protocol, in slices prepared during the L-phase. **(F)** As in (E), in slices prepared during the D-phase. **(G)** Quantification of the proExM-induced perimeter increase in hippocampal slices.

Figure 11. Astrocytes cover a similar area of the neuropil during the L/D-phases. (A) Maximum intensity projection of biocytin-filled astrocytes collected using confocal microscopy. **(B)** Maximum intensity projection of the same astrocytes after proExM collected using 2P-LSM. **(C)** Polar plots of astrocyte contours after confocal imaging. **(D)** Polar plots of astrocyte contours after proExM and 2P-LSM. **(E)** Polar plots showing the average contour of astrocytes during the L/D-phases. **(F)** Polar plot showing the average contour of astrocytes after proExM. **(G)** Summary graph of astrocyte surface area. **(H)** As in (G), after proExM.

Figure 12. Astrocytes reduce the number of their fine processes during the D-phase. (A) Axial STEM tomography reconstruction of hippocampal processes (blue) and PSDs (red) in *stratum radiatum* of a hippocampal slice prepared during the L-phase. **(B)** As in (A), for the D-phase. **(C)** Astrocytic processes have similar volume in the L/D-phases. The box and whisker plots show the median (thick central line), 25th-75th percentile (box top and bottom) and 10th-90th percentile (whisker top and bottom). **(D)** Astrocytic processes have similar surface area in the L/D-phases. **(E)** The distance between PSDs and their nearest neighboring astrocyte was increased during the D-phase. **(F)** The PSD surface area did not change during the L/D-phases. **(G)** *Left,* maximum intensity projection of pre-processed confocal z-stacks. *Right,* segmentation of the projection for Sholl analysis with probabilistic thresholding using anisotropic filters.

The probabilistic thresholding procedure relied on the following steps. *First,* the input image was mixed with additive Gaussian noise then convolved by a filter bank of isotropic and anisotropic high-pass filters. *Second*, responses to isotropic and highest-amplitude responses to anisotropic filters were thresholded. This procedure was repeated 20 times, and the probabilities of the pixel to be "on" in filter responses are shown as color maps. **(H)** As in G, for biocytin-filled neurons in slices prepared at ZT15.5 (D-phase). **(I)** The Sholl analysis of astrocytes showed that astrocytes have fewer distal processes during the D-phase. **(J)** Summary of the total number of intersections measured by the Sholl analysis using concentric circles centered at the soma, with radii that increased progressively in 1 µm steps. The total number of intersections was reduced during the D-phase. **(K)** Entropy and complexity values for each cell, normalized by the corresponding entropy values in the neuropil around them. The normalized entropy was smaller during the D-phase. In contrast, the normalized complexity was increased during the D-phase.

References

Attwell D, Laughlin SB (2001) An energy budget for signaling in the grey matter of the brain. J Cereb Blood Flow Metab 21:1133-1145.

Barnes CA, McNaughton BL, Goddard GV, Douglas RM, Adamec R (1977) Circadian rhythm of synaptic excitability in rat and monkey central nervous system. Science 197:91-92.

Benitez-King G, Hernandez ME, Tovar R, Ramirez G (2001) Melatonin activates PKC-alpha but not PKC-epsilon in N1E-115 cells. Neurochemistry International 39:95-102.

BenitezKing G, Rios A, Martinez A, AntonTay F (1996) In vitro inhibition of Ca2+/calmodulin-dependent kinase II activity by melatonin. Bba-Gen Subjects 1290:191-196.

Brancaccio M, Patton AP, Chesham JE, Maywood ES, Hastings MH (2017) Astrocytes Control Circadian Timekeeping in the Suprachiasmatic Nucleus via Glutamatergic Signaling. Neuron 93:1420-1435 e1425.

Brancaccio M, Edwards MD, Patton AP, Smyllie NJ, Chesham JE, Maywood ES, Hastings MH (2019) Cell-autonomous clock of astrocytes drives circadian behavior in mammals. Science 363:187-+.

Brazhe A (2018) Shearlet-based measures of entropy and complexity for two-dimensional patterns. Phys Rev E 97.

Buzsaki G (2002) Theta oscillations in the hippocampus. Neuron 33:325-340.

Carlberg C, Wiesenberg I (1995) The Orphan Receptor Family Rzr/Ror, Melatonin and 5-Lipoxygenase - an Unexpected Relationship. J Pineal Res 18:171-178.

Chaudhury D, Colwell CS (2002) Circadian modulation of learning and memory in fear-conditioned mice. Behav Brain Res 133:95-108.

Chung S, Son GH, Kim K (2011) Circadian rhythm of adrenal glucocorticoid: its regulation and clinical implications. Biochim Biophys Acta 1812:581-591.

Collins DR, Davies SN (1997) Melatonin blocks the induction of long-term potentiation in an N-methyl-D-aspartate independent manner. Brain Res 767:162-165.

Cotte Y, Toy F, Jourdain P, Pavillon N, Boss D, Magistretti P, Marquet P, Depeursinge C (2013) Marker-free phase nanoscopy. Nat Photonics 7:113-117.

Debski KJ, Ceglia N, Ghestem A, Ivanov AI, Brancati GE, Bröer S, Bot AM, Müller JA, Schoch S, Becker A, Löscher W, Sassone-Corsi P, Lukasiuk K, Baldi P, Bernard C (2017) The circadian hippocampus and its reprogramming in epilepsy: impact for chronotherapeutics. bioRxiv.

Diamond JS (2005) Deriving the glutamate clearance time course from transporter currents in CA1 hippocampal astrocytes: transmitter uptake gets faster during development. J Neurosci 25:2906-2916.

Dickmeis T (2009) Glucocorticoids and the circadian clock. J Endocrinol 200:3-22.

Dubocovich ML (2007) Melatonin receptors: Role on sleep and circadian rhythm regulation. Sleep Med 8:S34-S42.

Dubocovich ML, Rivera-Bermudez MA, Gerdin MJ, Masana MI (2003) Molecular pharmacology, regulation and function of mammalian melatonin receptors. Front Biosci 8:d1093-1108.

Ebihara S, Marks T, Hudson DJ, Menaker M (1986) Genetic-Control of Melatonin Synthesis in the Pineal-Gland of the Mouse. Science 231:491-493.

Engert F, Bonhoeffer T (1999) Dendritic spine changes associated with hippocampal long-term synaptic plasticity. Nature 399:66-70.

Gasparini S, Migliore M, Magee JC (2004) On the initiation and propagation of dendritic spikes in CA1 pyramidal neurons. J Neurosci 24:11046-11056.

Gavrilov N, Golyagina I, Brazhe A, Scimemi A, Turlapov V, Semyanov A (2018) Astrocytic Coverage of Dendritic Spines, Dendritic Shafts, and Axonal Boutons in Hippocampal Neuropil. Front Cell Neurosci 12:248.

Gerstner JR, Lyons LC, Wright KP, Jr., Loh DH, Rawashdeh O, Eckel-Mahan KL, Roman GW (2009) Cycling behavior and memory formation. J Neurosci 29:12824-12830.

Gilbert CD (1998) Adult cortical dynamics. Physiological Reviews 78:467-485.
Guilding C, Piggins HD (2007) Challenging the omnipotence of the suprachiasmatic timekeeper: are circadian oscillators present throughout the mammalian brain? Eur J Neurosci 25:3195-3216.
Guo K, Labate D (2007) Optimally sparse multidimensional representation using shearlets. Siam J Math Anal 39:298-318.
Haber M, Zhou L, Murai KK (2006) Cooperative astrocyte and dendritic spine dynamics at hippocampal excitatory synapses. Journal of Neuroscience 26:8881-8891.
Harris KM, Teyler TJ (1983) Age differences in a circadian influence on hippocampal LTP. Brain Res 261:69-73.
Hines ML, Carnevale NT (1997) The NEURON simulation environment. Neural Comput 9:1179-1209.
Hirrlinger J, Hulsmann S, Kirchhoff F (2004) Astroglial processes show spontaneous motility at active synaptic terminals in situ. European Journal of Neuroscience 20:2235-2239.
Hohmann-Marriott MF, Sousa AA, Azari AA, Glushakova S, Zhang G, Zimmerberg J, Leapman RD (2009) Nanoscale 3D cellular imaging by axial scanning transmission electron tomography. Nat Methods 6:729-731.
Holtmaat AJGD, Trachtenberg JT, Wilbrecht L, Shepherd GM, Zhang XQ, Knott GW, Svoboda K (2005) Transient and persistent dendritic spines in the neocortex in vivo. Neuron 45:279-291.
Huettner JE (1989) Indole-2-Carboxylic Acid - a Competitive Antagonist of Potentiation by Glycine at the Nmda Receptor. Science 243:1611-1613.
Hui GK, Figueroa IR, Poytress BS, Roozendaal B, McGaugh JL, Weinberger NM (2004) Memory enhancement of classical fear conditioning by post-training injections of corticosterone in rats. Neurobiol Learn Mem 81:67-74.
Ishida A, Mutoh T, Ueyama T, Bando H, Masubuchi S, Nakahara D, Tsujimoto G, Okamura H (2005) Light activates the adrenal gland: Timing of gene expression and glucocorticoid release. Cell Metabolism 2:297-307.
Jiao YY, Lee TM, Rusak B (1999) Photic responses of suprachiasmatic area neurons in diurnal degus (Octodon degus) and nocturnal rats (Rattus norvegicus). Brain Research 817:93-103.
Jonas P, Major G, Sakmann B (1993) Quantal Components of Unitary Epscs at the Mossy Fiber Synapse on Ca3 Pyramidal Cells of Rat Hippocampus. J Physiol-London 472:615-663.
Kalsbeek A, Buijs RM (2002) Output pathways of the mammalian suprachiasmatic nucleus: coding circadian time by transmitter selection and specific targeting. Cell Tissue Res 309:109-118.
Kasahara T, Abe K, Mekada K, Yoshiki A, Kato T (2010) Genetic variation of melatonin productivity in laboratory mice under domestication. Proc Natl Acad Sci U S A 107:6412-6417.
Katagiri H, Tanaka K, Manabe T (2001) Requirement of appropriate glutamate concentrations in the synaptic cleft for hippocampal LTP induction. European Journal of Neuroscience 14:547-553.
Kim JJ, Yoon KS (1998) Stress: metaplastic effects in the hippocampus. Trends Neurosci 21:505-509.
Kwon HB, Sabatini BL (2011) Glutamate induces de novo growth of functional spines in developing cortex. Nature 474:100-104.
Lamberti PW, Martin MT, Plastino A, Rosso OA (2004) Intensive entropic non-triviality measure. Physica A 334:119-131.
Lavialle M, Aumann G, Anlauf E, Prols F, Arpin M, Derouiche A (2011) Structural plasticity of perisynaptic astrocyte processes involves ezrin and metabotropic glutamate receptors. P Natl Acad Sci USA 108:12915-12919.
Lehman MN, Silver R, Gladstone WR, Kahn RM, Gibson M, Bittman EL (1987) Circadian rhythmicity restored by neural transplant. Immunocytochemical characterization of the graft and its integration with the host brain. J Neurosci 7:1626-1638.
Lester RAJ, Jahr CE (1992) Nmda Channel Behavior Depends on Agonist Affinity. Journal of Neuroscience 12:635-643.

Longair MH, Baker DA, Armstrong JD (2011) Simple Neurite Tracer: open source software for reconstruction, visualization and analysis of neuronal processes. Bioinformatics 27:2453-2454.
Marr D (1971) Simple memory: a theory for archicortex. Philos Trans R Soc Lond B Biol Sci 262:23-81.
Meijer JH, Watanabe K, Schaap J, Albus H, Detari L (1998) Light responsiveness of the suprachiasmatic nucleus: long-term multiunit and single-unit recordings in freely moving rats. J Neurosci 18:9078-9087.
Meyer-Bernstein EL, Jetton AE, Matsumoto SI, Markuns JF, Lehman MN, Bittman EL (1999) Effects of suprachiasmatic transplants on circadian rhythms of neuroendocrine function in golden hamsters. Endocrinology 140:207-218.
Migliore M, Shepherd GM (2002) Emerging rules for the distributions of active dendritic conductances. Nat Rev Neurosci 3:362-370.
Migliore M, De Simone G, Migliore R (2015) Effect of the initial synaptic state on the probability to induce long-term potentiation and depression. Biophys J 108:1038-1046.
Migliore R et al. (2018) The physiological variability of channel density in hippocampal CA1 pyramidal cells and interneurons explored using a unified data-driven modeling workflow. PLoS Comput Biol 14:e1006423.
Moore RY (1996) Neural control of the pineal gland. Behav Brain Res 73:125-130.
Moore RY, Lenn NJ (1972) A retinohypothalamic projection in the rat. J Comp Neurol 146:1-14.
Namihira M, Honma S, Abe H, Tanahashi Y, Ikeda M, Honma K (1999) Daily variation and light responsiveness of mammalian clock gene, Clock and BMAL1, transcripts in the pineal body and different areas of brain in rats. Neurosci Lett 267:69-72.
Nishida H, Okabe S (2007) Direct astrocytic contacts regulate local maturation of dendritic spines. Journal of Neuroscience 27:331-340.
Ozcan M, Yilmaz B, Carpenter DO (2006) Effects of melatonin on synaptic transmission and long-term potentiation in two areas of mouse hippocampus. Brain Research 1111:90-94.
Papouin T, Dunphy JM, Tolman M, Dineley KT, Haydon PG (2017) Septal Cholinergic Neuromodulation Tunes the Astrocyte-Dependent Gating of Hippocampal NMDA Receptors to Wakefulness. Neuron 94:840-854 e847.
Pavlides C, Watanabe Y, Magarinos AM, McEwen BS (1995) Opposing roles of type I and type II adrenal steroid receptors in hippocampal long-term potentiation. Neuroscience 68:387-394.
Peirson SN, Brown LA, Pothecary CA, Benson LA, Fisk AS (2018) Light and the laboratory mouse. J Neurosci Meth 300:26-36.
Prolo LM, Takahashi JS, Herzog ED (2005) Circadian rhythm generation and entrainment in astrocytes. Journal of Neuroscience 25:404-408.
Rafii-El-Idrissi M, Calvo JR, Harmouch A, Garcia-Maurino S, Guerrero JM (1998) Specific binding of melatonin by purified cell nuclei from spleen and thymus of the rat. J Neuroimmunol 86:190-197.
Raghavan AV, Horowitz JM, Fuller CA (1999) Diurnal modulation of long-term potentiation in the hamster hippocampal slice. Brain Res 833:311-314.
Rakic P, Bourgeois JP, Eckenhoff MF, Zecevic N, Goldmanrakic PS (1986) Concurrent Overproduction of Synapses in Diverse Regions of the Primate Cerebral-Cortex. Science 232:232-235.
Rawashdeh O, Parsons R, Maronde E (2018) Clocking In Time to Gate Memory Processes: The Circadian Clock Is Part of the Ins and Outs of Memory. Neural Plast.
Rawashdeh O, de Borsetti NH, Roman G, Cahill GM (2007) Melatonin suppresses nighttime memory formation in zebrafish. Science 318:1144-1146.
Reichenbach A, Derouiche A, Kirchhoff F (2010) Morphology and dynamics of perisynaptic glia. Brain Research Reviews 63:11-25.
Reick M, Garcia JA, Dudley C, McKnight SL (2001) NPAS2: an analog of clock operative in the mammalian forebrain. Science 293:506-509.

Reppert SM, Weaver DR, Godson C (1996) Melatonin receptors step into the light: Cloning and classification of subtypes. Trends Pharmacol Sci 17:100-102.

Richards DA, Mateos JM, Hugel S, de Paola V, Caroni P, Gahwiler BH, McKinney RA (2005) Glutamate induces the rapid formation of spine head protrusions in hippocampal slice cultures. P Natl Acad Sci USA 102:6166-6171.

Rosso OA, Larrondo HA, Martin MT, Plastino A, Fuentes MA (2007) Distinguishing noise from chaos. Phys Rev Lett 99.

Ruby NF, Hwang CE, Wessells C, Fernandez F, Zhang P, Sapolsky R, Heller HC (2008) Hippocampal-dependent learning requires a functional circadian system. P Natl Acad Sci USA 105:15593-15598.

Salituro FG, Harrison BL, Baron BM, Nyce PL, Stewart KT, Mcdonald IA (1990) 3-(2-Carboxyindol-3-Yl)Propionic Acid-Derivatives - Antagonists of the Strychnine-Insensitive Glycine Receptor Associated with the N-Methyl-D-Aspartate Receptor Complex. J Med Chem 33:2944-2946.

Salituro FG, Harrison BL, Baron BM, Nyce PL, Stewart KT, Kehne JH, White HS, Mcdonald IA (1992) 3-(2-Carboxyindol-3-Yl)Propionic Acid-Based Antagonists of the N-Methyl-D-Aspartic Acid Receptor Associated Glycine Binding-Site. J Med Chem 35:1791-1799.

Saunders A, Macosko EZ, Wysoker A, Goldman M, Krienen FM, de Rivera H, Bien E, Baum M, Bortolin L, Wang SY, Goeva A, Nemesh J, Kamitaki N, Brumbaugh S, Kulp D, McCarroll SA (2018) Molecular Diversity and Specializations among the Cells of the Adult Mouse Brain. Cell 174:1015-+.

Scimemi A, Diamond JS (2013) Deriving the time course of glutamate clearance with a deconvolution analysis of astrocytic transporter currents. J Vis Exp.

Scimemi A, Tian H, Diamond JS (2009) Neuronal transporters regulate glutamate clearance, NMDA receptor activation, and synaptic plasticity in the hippocampus. J Neurosci 29:14581-14595.

Scimemi A, Meabon JS, Woltjer RL, Sullivan JM, Diamond JS, Cook DG (2013) Amyloid-beta1-42 slows clearance of synaptically released glutamate by mislocalizing astrocytic GLT-1. J Neurosci 33:5312-5318.

Shimizu K, Kobayashi Y, Nakatsuji E, Yamazaki M, Shimba S, Sakimura K, Fukada Y (2016) SCOP/PHLPP1beta mediates circadian regulation of long-term recognition memory. Nat Commun 7:12926.

Smale L, Lee T, Nunez AA (2003) Mammalian diurnality: Some facts and gaps. J Biol Rhythm 18:356-366.

Smarr BL, Jennings KJ, Driscoll JR, Kriegsfeld LJ (2014) A time to remember: the role of circadian clocks in learning and memory. Behav Neurosci 128:283-303.

Snider KH, Dziema H, Aten S, Loeser J, Norona FE, Hoyt K, Obrietan K (2016) Modulation of learning and memory by the targeted deletion of the circadian clock gene Bmal1 in forebrain circuits. Behav Brain Res 308:222-235.

Sousa AA, Azari AA, Zhang G, Leapman RD (2011) Dual-axis electron tomography of biological specimens: Extending the limits of specimen thickness with bright-field STEM imaging. J Struct Biol 174:107-114.

Stephan FK, Zucker I (1972) Circadian rhythms in drinking behavior and locomotor activity of rats are eliminated by hypothalamic lesions. Proc Natl Acad Sci U S A 69:1583-1586.

Sumova A, Sladek M, Polidarova L, Novakova M, Houdek P (2012) Circadian system from conception till adulthood. Prog Brain Res 199:83-103.

Sumova A, Bendova Z, Sladek M, El-Hennamy R, Mateju K, Polidarova L, Sosniyenko S, Illnerova H (2008) Circadian Molecular Clocks Tick along Ontogenesis. Physiol Res 57:S139-S148.

Sweeney AM, Fleming KE, McCauley JP, Rodriguez MF, Martin ET, Sousa AA, Leapman RD, Scimemi A (2017) PAR1 activation induces rapid changes in glutamate uptake and astrocyte morphology. Sci Rep 7:43606.

Tillberg PW, Chen F, Piatkevich KD, Zhao Y, Yu CC, English BP, Gao L, Martorell A, Suk HJ, Yoshida F, DeGennaro EM, Roossien DH, Gong G, Seneviratne U, Tannenbaum SR, Desimone R, Cai D, Boyden ES

(2016) Protein-retention expansion microscopy of cells and tissues labeled using standard fluorescent proteins and antibodies. Nat Biotechnol 34:987-992.
Tsodyks M, Pawelzik K, Markram H (1998) Neural networks with dynamic synapses. Neural Comput 10:821-835.
Vanecek J (1998) Cellular mechanisms of melatonin action. Physiol Rev 78:687-721.
Wakamatsu H, Yoshinobu Y, Aida R, Moriya T, Akiyama M, Shibata S (2001) Restricted-feeding-induced anticipatory activity rhythm is associated with a phase-shift of the expression of mPer1 and mPer2 mRNA in the cerebral cortex and hippocampus but not in the suprachiasmatic nucleus of mice. European Journal of Neuroscience 13:1190-1196.
Wang LM, Suthana NA, Chaudhury D, Weaver DR, Colwell CS (2005) Melatonin inhibits hippocampal long-term potentiation. Eur J Neurosci 22:2231-2237.
Weickert J, Scharr H (2002) A scheme for coherence-enhancing diffusion filtering with optimized rotation invariance. J Vis Commun Image R 13:103-118.
Weinert D (2005) Ontogenetic development of the mammalian circadian system. Chronobiol Int 22:179-205.
Whitehead G, Jo J, Hogg EL, Piers T, Kim DH, Seaton G, Seok H, Bru-Mercier G, Son GH, Regan P, Hildebrandt L, Waite E, Kim BC, Kerrigan TL, Kim K, Whitcomb DJ, Collingridge GL, Lightman SL, Cho K (2013) Acute stress causes rapid synaptic insertion of Ca2+-permeable AMPA receptors to facilitate long-term potentiation in the hippocampus. Brain 136:3753-3765.
Willshaw DJ, Dayan P, Morris RG (2015) Memory, modelling and Marr: a commentary on Marr (1971) 'Simple memory: a theory of archicortex'. Philos Trans R Soc Lond B Biol Sci 370.
Winson J, Abzug C (1977) Gating of neuronal transmission in the hippocampus: efficacy of transmission varies with behavioral state. Science 196:1223-1225.
Winson J, Abzug C (1978) Neuronal transmission through hippocampal pathways dependent on behavior. J Neurophysiol 41:716-732.
Yuen EY, Liu W, Karatsoreos IN, Ren Y, Feng J, McEwen BS, Yan Z (2011) Mechanisms for acute stress-induced enhancement of glutamatergic transmission and working memory. Mol Psychiatr 16:156-170.
Zerangue N, Kavanaugh MP (1996) Flux coupling in a neuronal glutamate transporter. Nature 383:634-637.

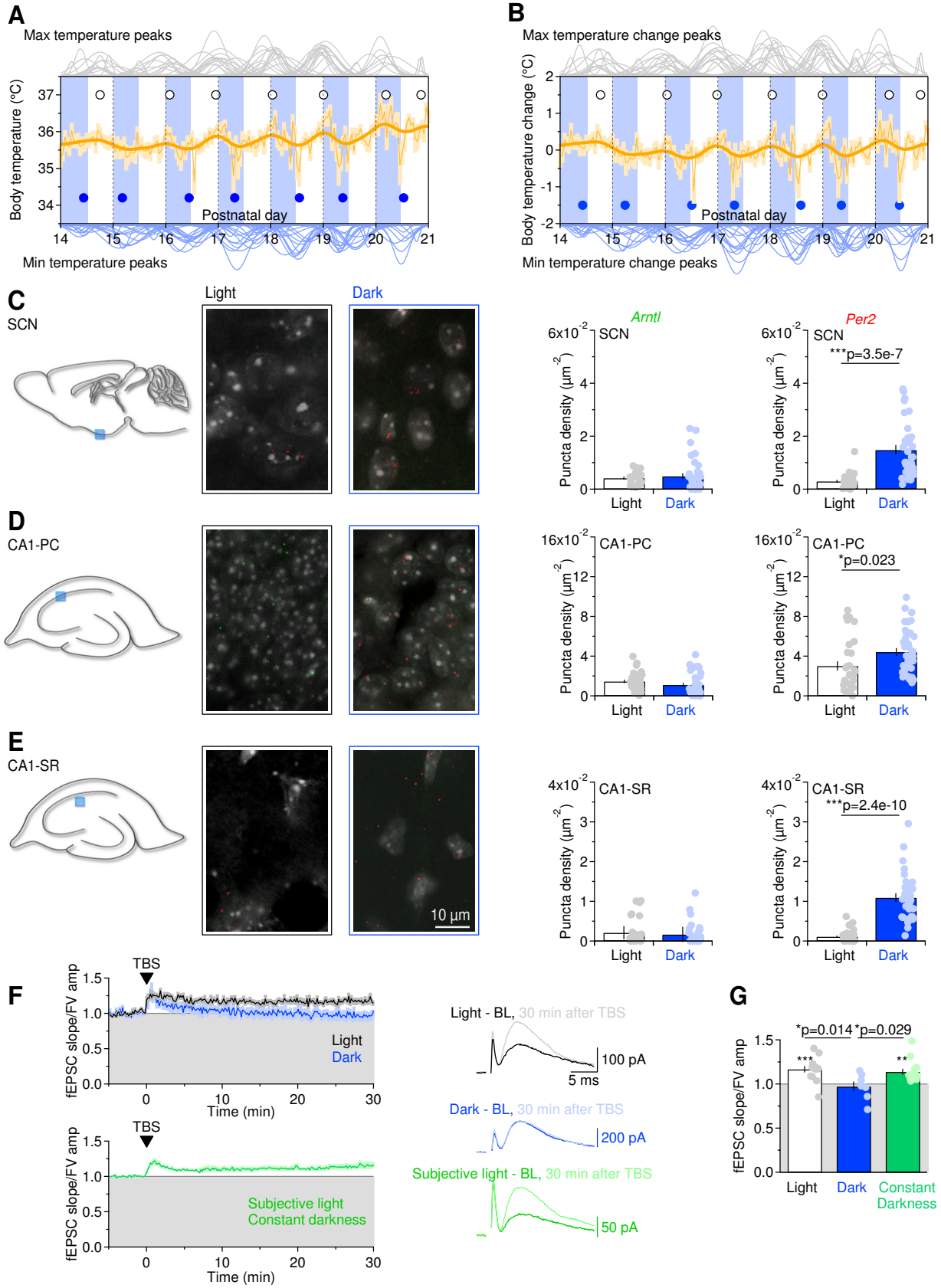
A
Max temperature peaks
Body temperature (°C)
Postnatal day
Min temperature peaks
B
Max temperature change peaks
Body temperature change (°C)
Postnatal day
Min temperature change peaks
C
SCN
Light
Dark
Arntl
Per2
Puncta density (µm-2)
***p=3.5e-7
D
CA1-PC
*p=0.023
E
CA1-SR
10 µm
***p=2.4e-10
F
TBS
fEPSC slope/FV amp
Time (min)
Light
Dark
Subjective light
Constant darkness
Light - BL, 30 min after TBS
100 pA
5 ms
Dark - BL, 30 min after TBS
200 pA
Subjective light - BL, 30 min after TBS
50 pA
G
*p=0.014
*p=0.029
Constant Darkness

Figure 1

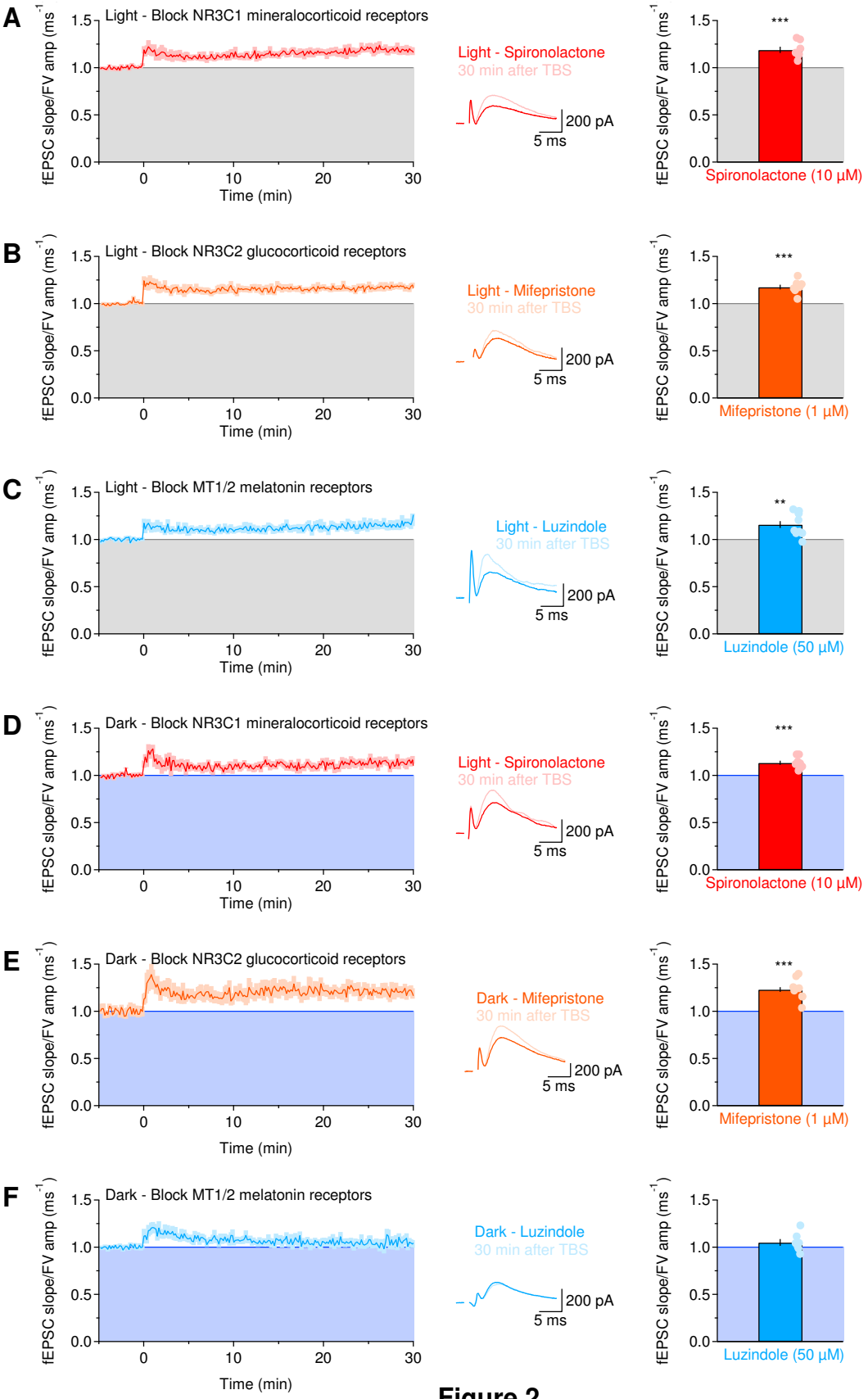
A
Light - Block NR3C1 mineralocorticoid receptors
fEPSC slope/FV amp (ms-1)
Time (min)
Light - Spironolactone
30 min after TBS
200 pA
5 ms
***
Spironolactone (10 μM)
B
Light - Block NR3C2 glucocorticoid receptors
Light - Mifepristone
30 min after TBS
Mifepristone (1 μM)
C
Light - Block MT1/2 melatonin receptors
Light - Luzindole
30 min after TBS
**
Luzindole (50 μM)
D
Dark - Block NR3C1 mineralocorticoid receptors
Light - Spironolactone
30 min after TBS
Spironolactone (10 μM)
E
Dark - Block NR3C2 glucocorticoid receptors
Dark - Mifepristone
30 min after TBS
Mifepristone (1 μM)
F
Dark - Block MT1/2 melatonin receptors
Dark - Luzindole
30 min after TBS
Luzindole (50 μM)

Figure 2

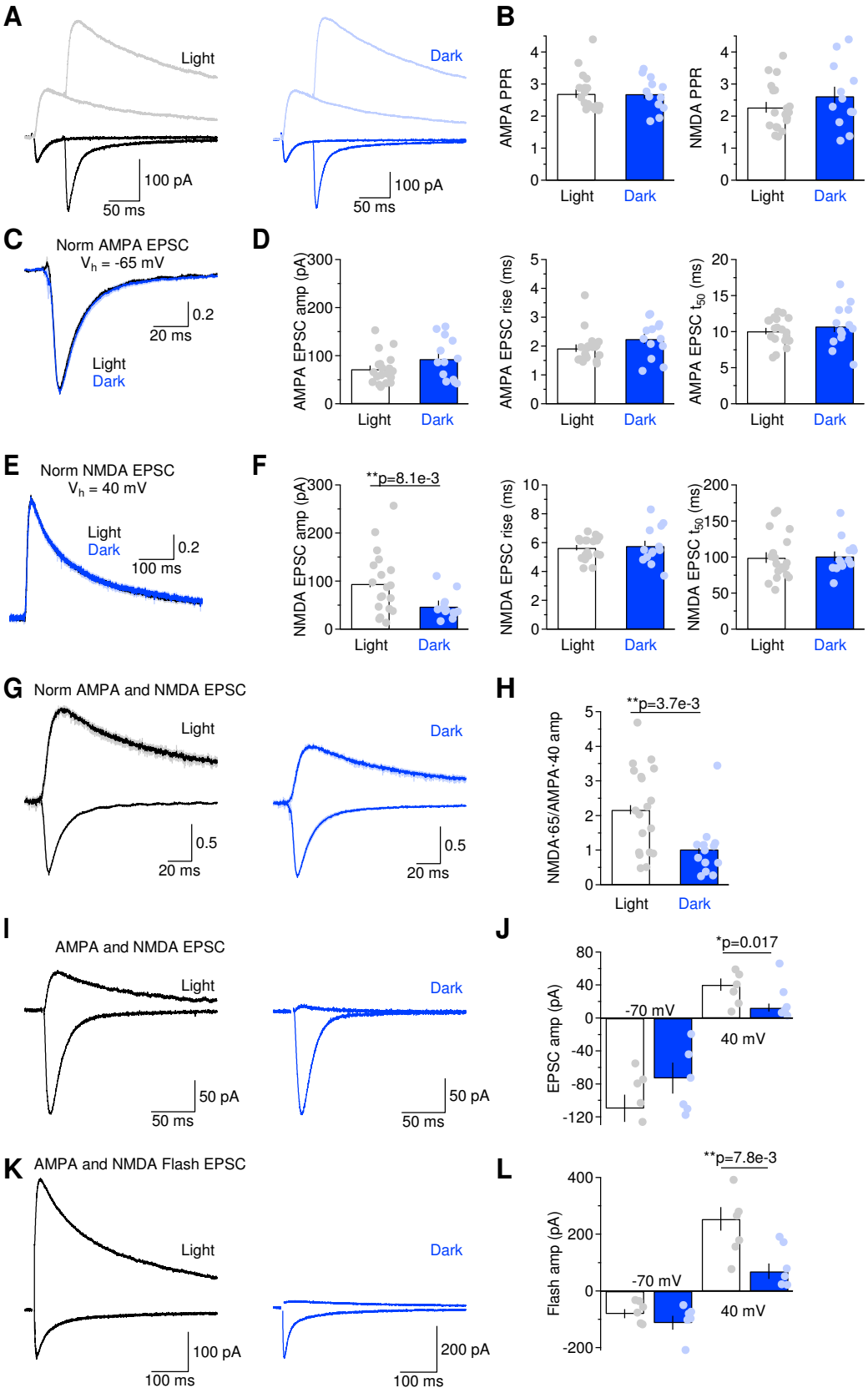
A
Light
Dark
100 pA
50 ms
B
AMPA PPR
NMDA PPR
Light
Dark
C
Norm AMPA EPSC
V_h = -65 mV
0.2
20 ms
Light
Dark
D
AMPA EPSC amp (pA)
AMPA EPSC rise (ms)
AMPA EPSC t_{50} (ms)
E
Norm NMDA EPSC
V_h = 40 mV
0.2
100 ms
F
**p=8.1e-3
NMDA EPSC amp (pA)
NMDA EPSC rise (ms)
NMDA EPSC t_{50} (ms)
G
Norm AMPA and NMDA EPSC
0.5
20 ms
H
**p=3.7e-3
NMDA-65/AMPA-40 amp
I
AMPA and NMDA EPSC
50 pA
50 ms
J
*p=0.017
-70 mV
40 mV
EPSC amp (pA)
K
AMPA and NMDA Flash EPSC
100 pA
100 ms
200 pA
L
**p=7.8e-3
Flash amp (pA)

Figure 3

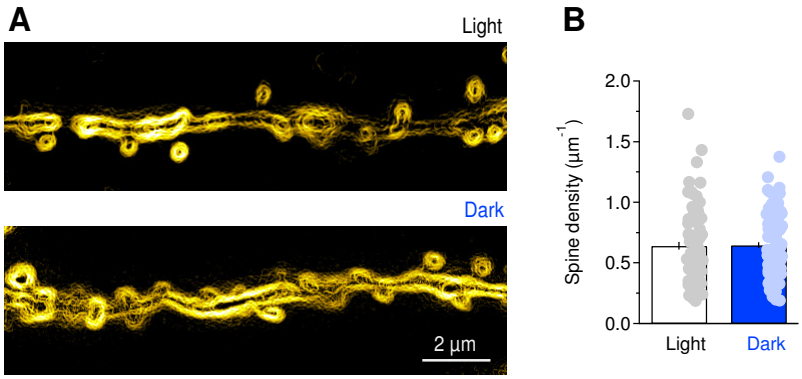

Figure 4

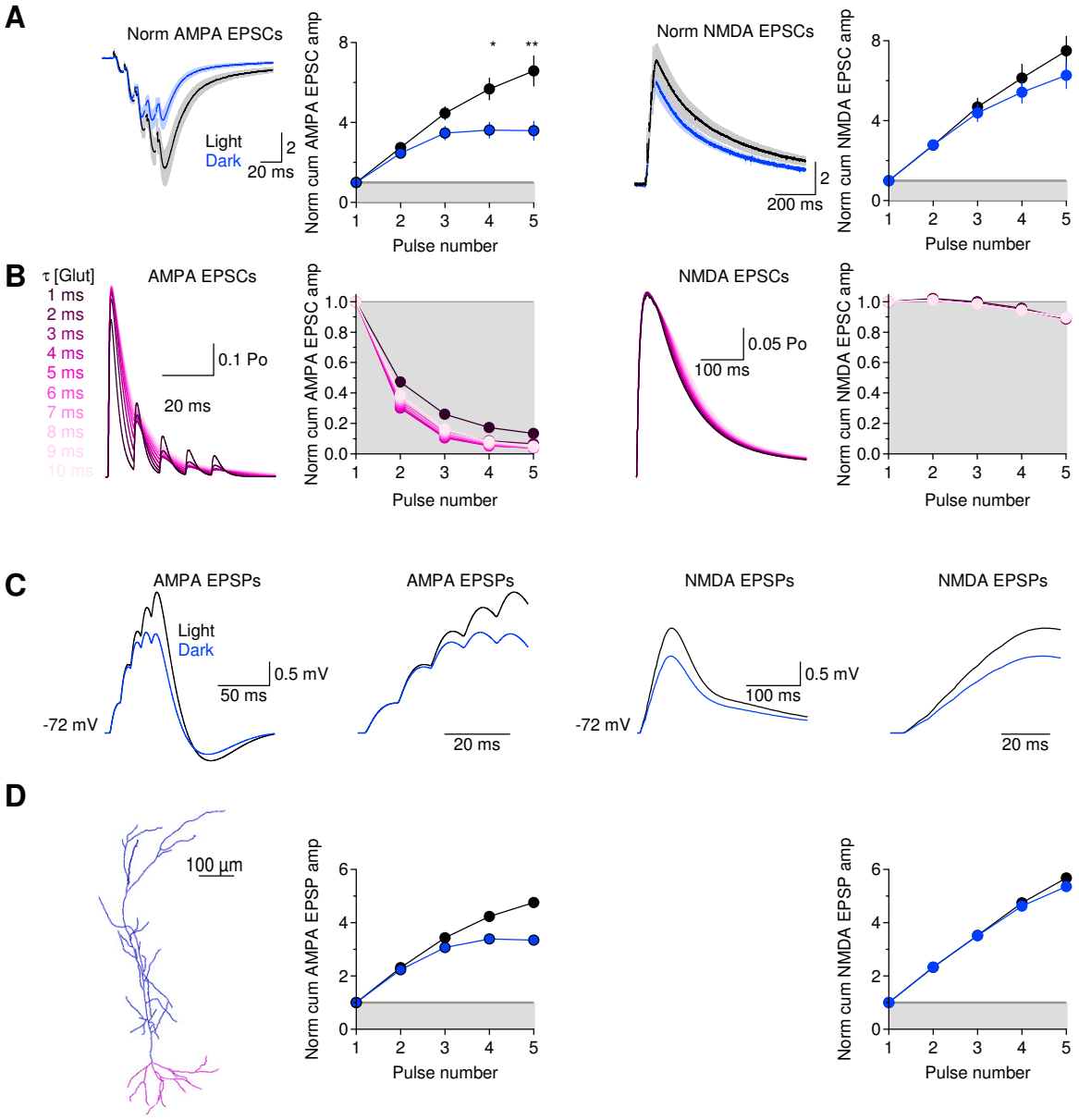
A
Norm AMPA EPSCs
Light
Dark
2
20 ms
Norm cum AMPA EPSC amp
Pulse number
Norm NMDA EPSCs
2
200 ms
Norm cum NMDA EPSC amp
Pulse number
B
τ [Glut]
1 ms
2 ms
3 ms
4 ms
5 ms
6 ms
7 ms
8 ms
9 ms
10 ms
AMPA EPSCs
0.1 Po
20 ms
Norm cum AMPA EPSC amp
Pulse number
NMDA EPSCs
0.05 Po
100 ms
Norm cum NMDA EPSC amp
Pulse number
C
AMPA EPSPs
Light
Dark
0.5 mV
50 ms
-72 mV
AMPA EPSPs
20 ms
NMDA EPSPs
0.5 mV
100 ms
-72 mV
NMDA EPSPs
20 ms
D
100 µm
Norm cum AMPA EPSP amp
Pulse number
Norm cum NMDA EPSP amp
Pulse number

Figure 5

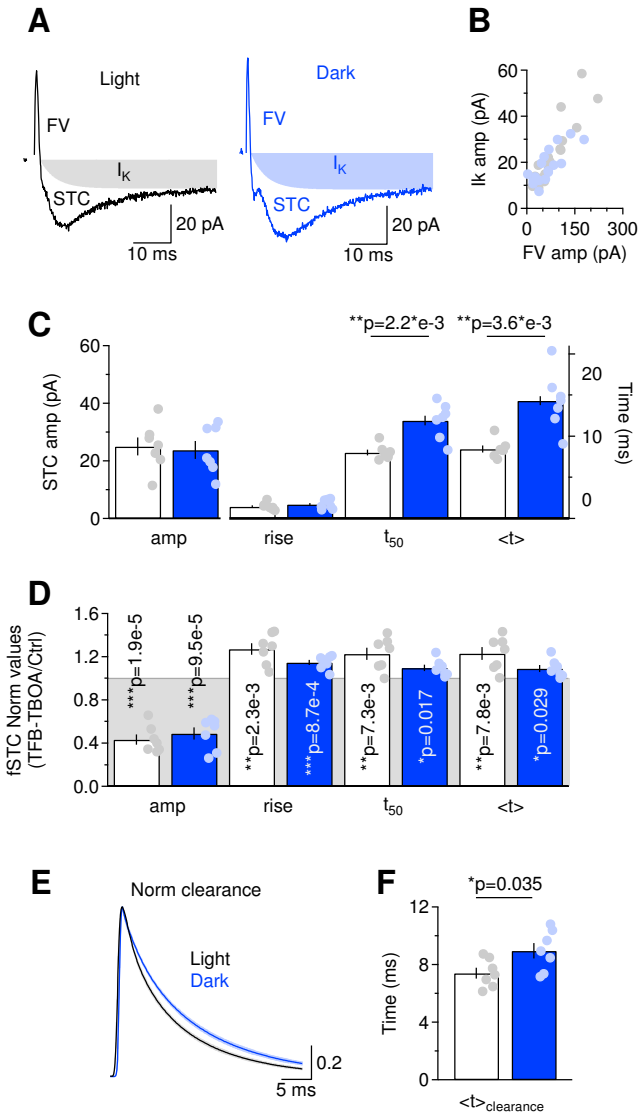
A
Light
FV
I_K
STC
20 pA
10 ms
Dark
FV
I_K
STC
20 pA
10 ms
B
Ik amp (pA)
60
40
20
0
0
150
300
FV amp (pA)
C
**p=2.2*e-3
**p=3.6*e-3
STC amp (pA)
60
40
20
0
Time (ms)
20
10
0
amp
rise
t_{50}
<t>
D
fSTC Norm values
(TFB-TBOA/Ctrl)
1.6
1.2
0.8
0.4
0.0
***p=1.9e-5
***p=9.5e-5
**p=2.3e-3
***p=8.7e-4
**p=7.3e-3
*p=0.017
**p=7.8e-3
*p=0.029
amp
rise
t_{50}
<t>
E
Norm clearance
Light
Dark
0.2
5 ms
F
*p=0.035
Time (ms)
12
8
4
0
$<t>_{clearance}$

Figure 6

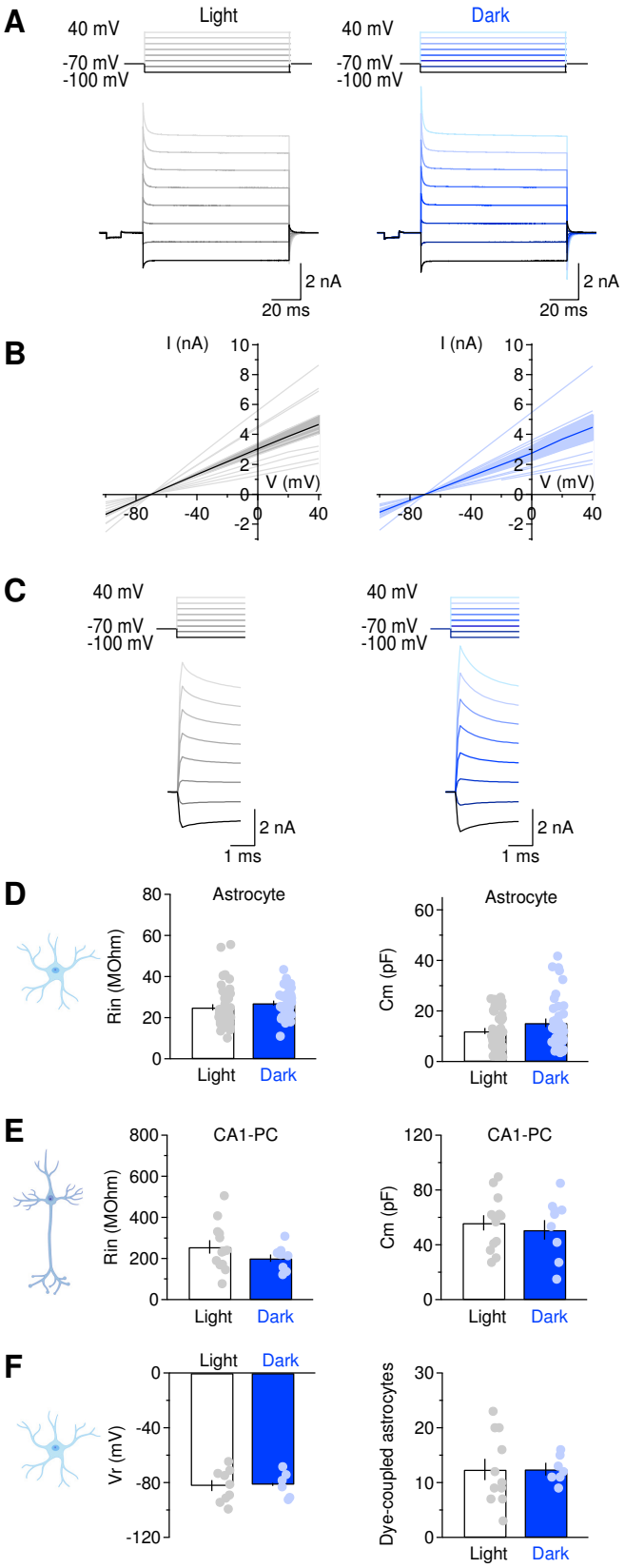
A
Light
Dark
40 mV
-70 mV
-100 mV
2 nA
20 ms
B
I (nA)
V (mV)
C
1 ms
D
Astrocyte
Rin (MOhm)
Cm (pF)
Light
Dark
E
CA1-PC
F
Vr (mV)
Dye-coupled astrocytes

Figure 7

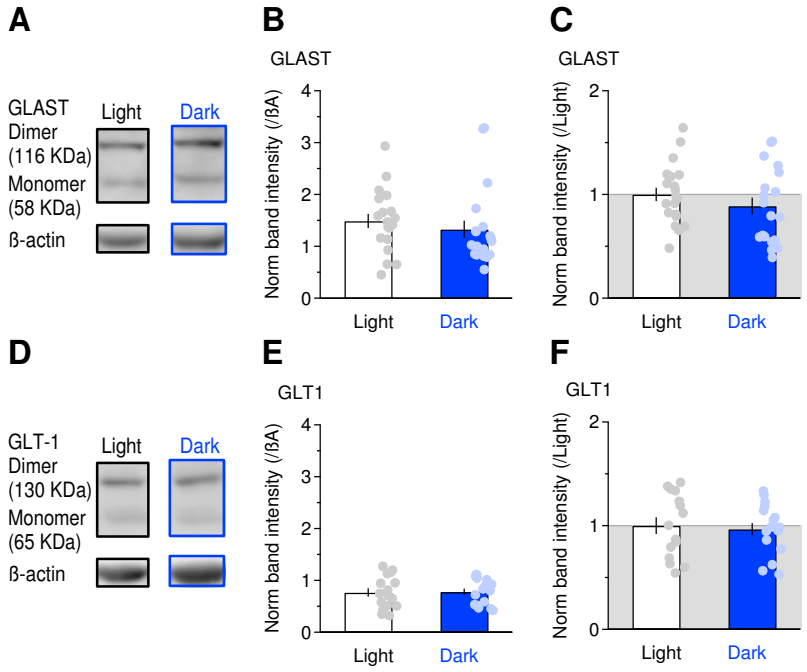
A
GLAST
Dimer
(116 KDa)
Monomer
(58 KDa)
ß-actin
Light
Dark
B
GLAST
Norm band intensity (/ßA)
0
1
2
3
4
Light
Dark
C
GLAST
Norm band intensity (/Light)
0
1
2
Light
Dark
D
GLT-1
Dimer
(130 KDa)
Monomer
(65 KDa)
ß-actin
Light
Dark
E
GLT1
Norm band intensity (/ßA)
0
1
2
3
4
Light
Dark
F
GLT1
Norm band intensity (/Light)
0
1
2
Light
Dark

Figure 8

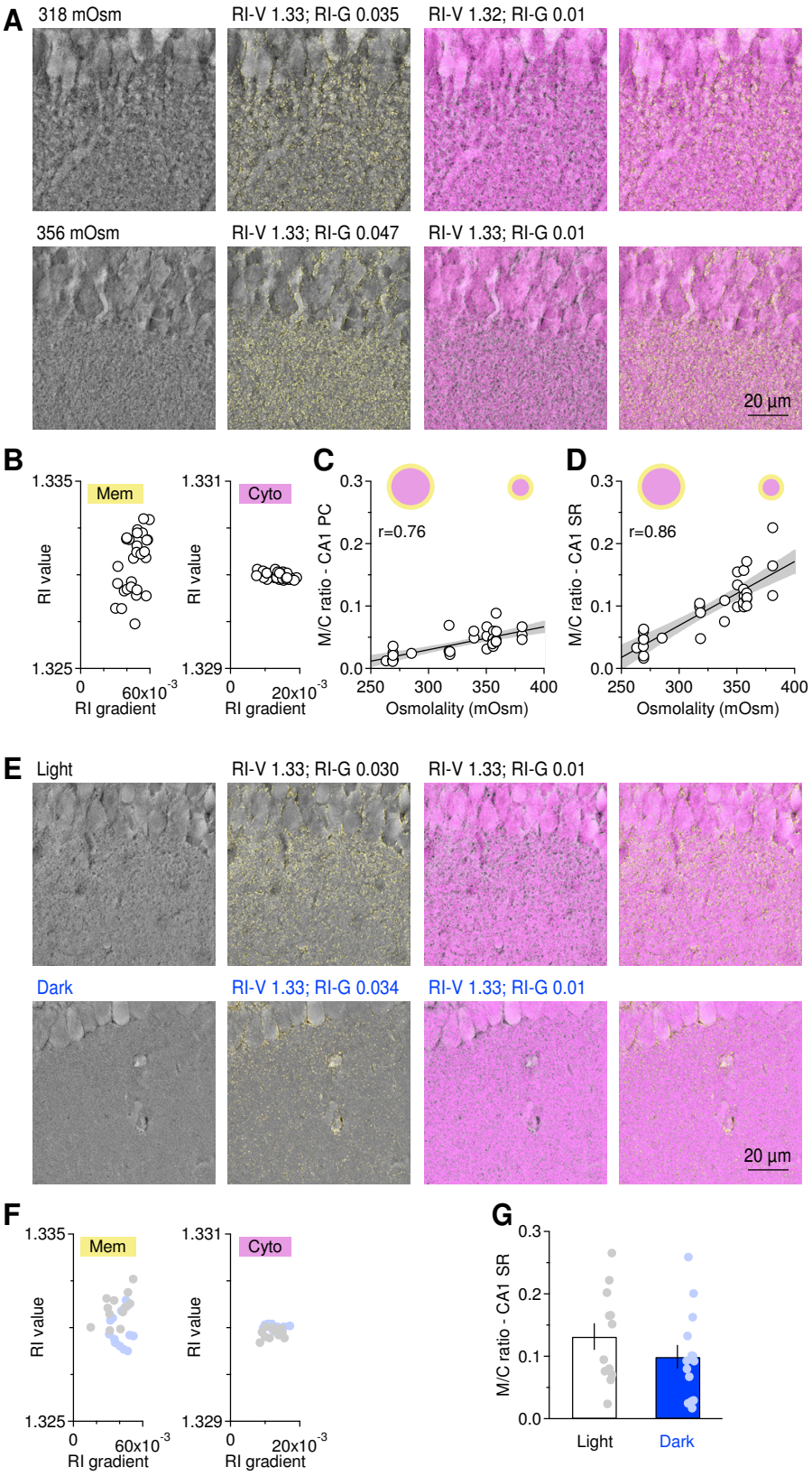
A
318 mOsm
RI-V 1.33; RI-G 0.035
RI-V 1.32; RI-G 0.01
356 mOsm
RI-V 1.33; RI-G 0.047
RI-V 1.33; RI-G 0.01
20 µm
B
Mem
Cyto
RI value
RI gradient
1.335
1.325
1.331
1.329
0
60x10-3
20x10-3
C
D
M/C ratio - CA1 PC
M/C ratio - CA1 SR
r=0.76
r=0.86
Osmolality (mOsm)
0.0
0.1
0.2
0.3
250
300
350
400
E
Light
RI-V 1.33; RI-G 0.030
RI-V 1.33; RI-G 0.01
Dark
RI-V 1.33; RI-G 0.034
RI-V 1.33; RI-G 0.01
20 µm
F
G
Light
Dark

Figure 9

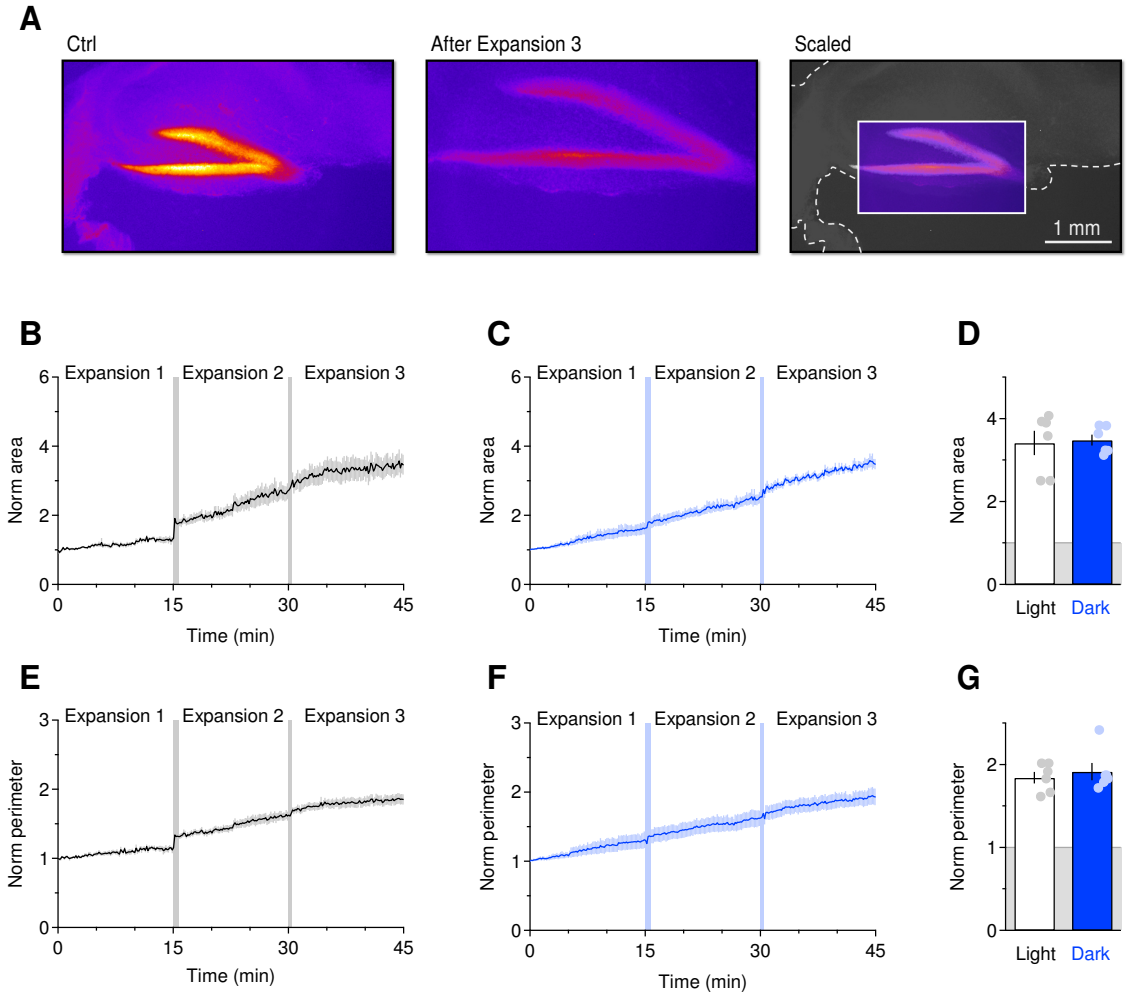
A
Ctrl
After Expansion 3
Scaled
1 mm
B
Expansion 1
Expansion 2
Expansion 3
Norm area
Time (min)
C
D
Light
Dark
E
Norm perimeter
F
G

Figure 10

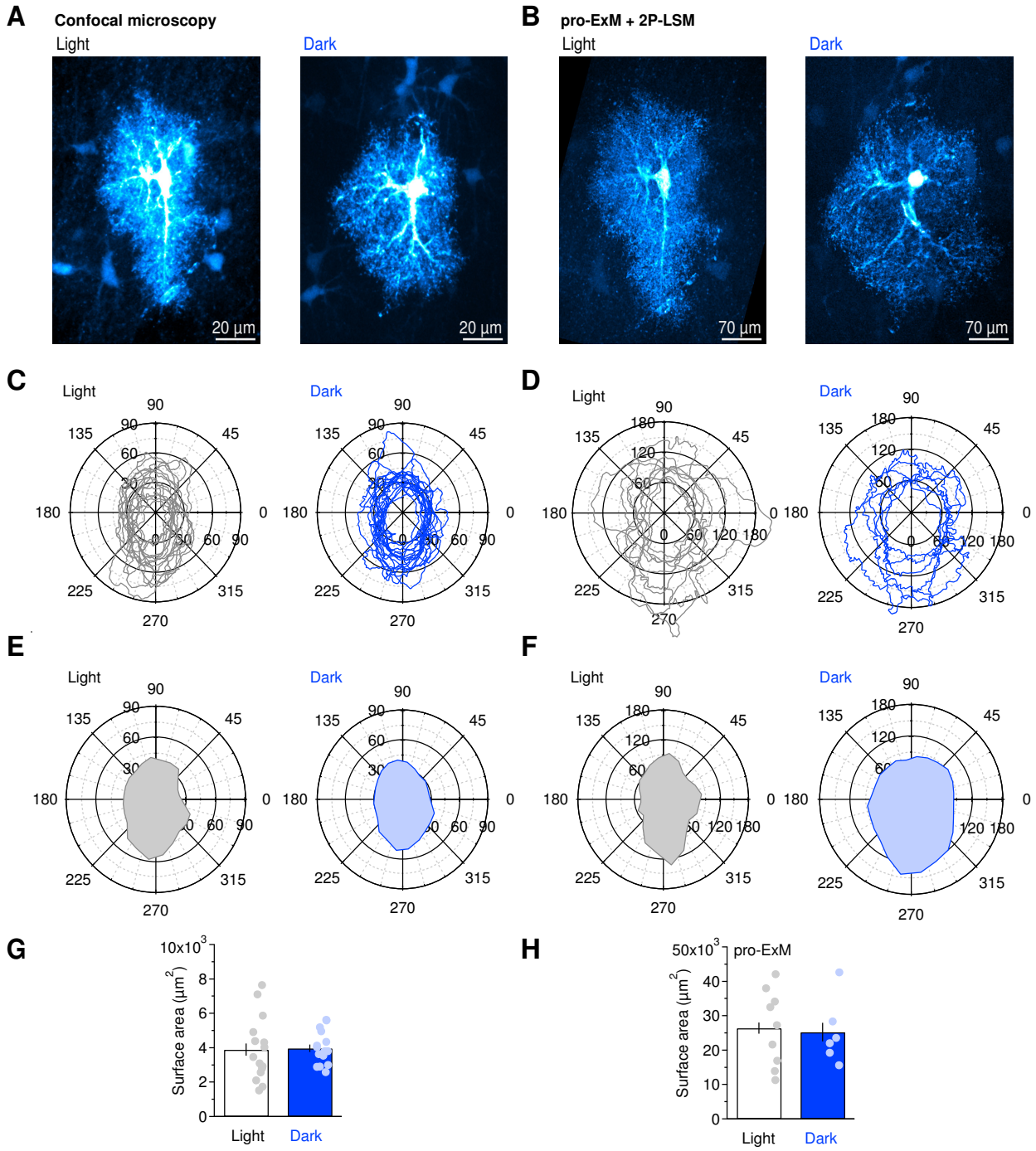
A
Confocal microscopy
Light
Dark
20 µm
20 µm
B
pro-ExM + 2P-LSM
Light
Dark
70 µm
70 µm
C
D
E
F
G
Surface area (µm²)
10x10³
Light
Dark
H
pro-ExM
50x10³
Surface area (µm²)
Light
Dark

Figure 11

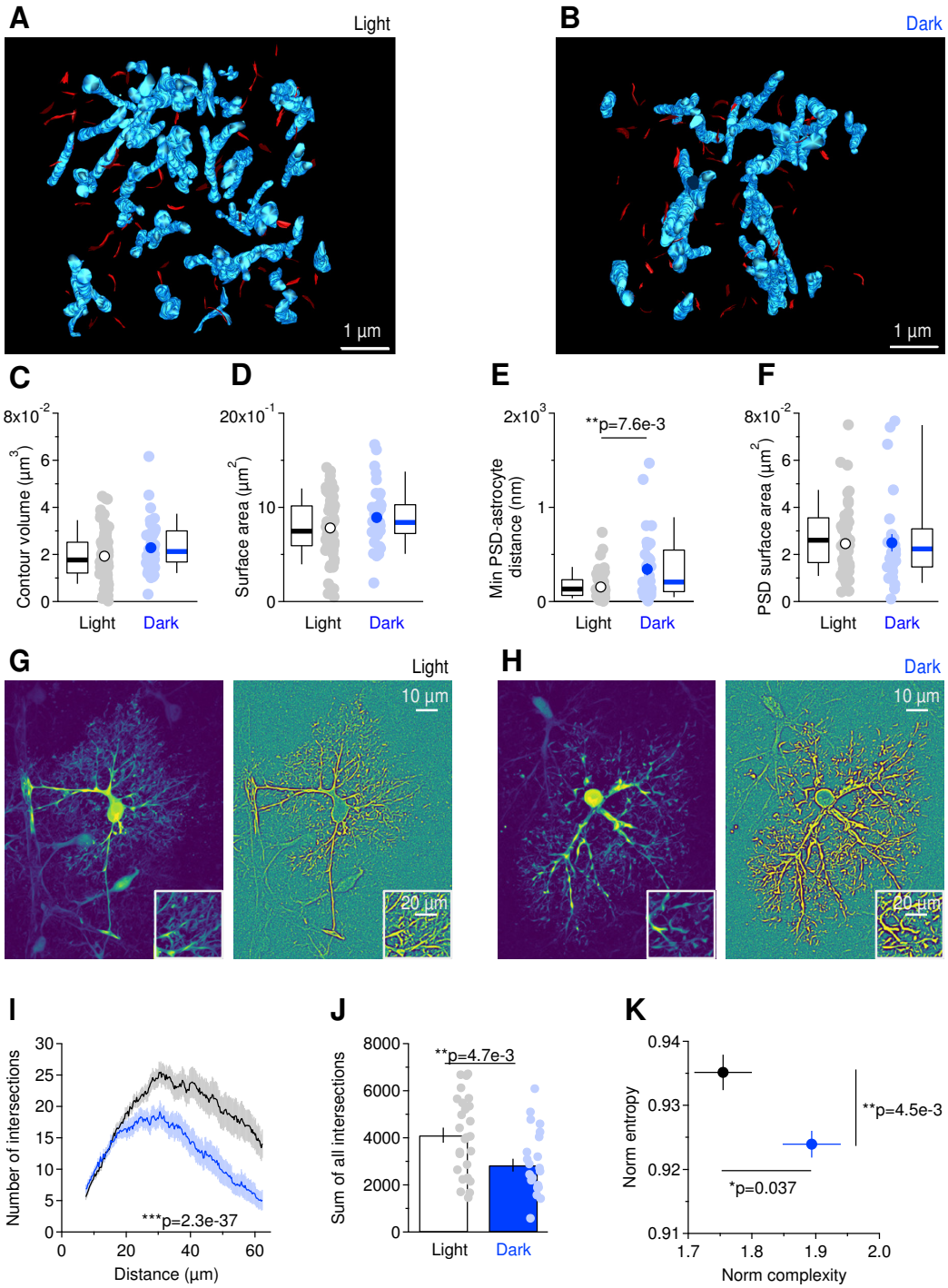
A
Light
1 µm
B
Dark
1 µm
C
8x10-2
Contour volume (µm3)
Light
Dark
D
20x10-1
Surface area (µm2)
Light
Dark
E
2x103
**p=7.6e-3
Min PSD-astrocyte distance (nm)
Light
Dark
F
8x10-2
PSD surface area (µm2)
Light
Dark
G
Light
10 µm
20 µm
H
Dark
10 µm
20 µm
I
Number of intersections
***p=2.3e-37
Distance (µm)
J
Sum of all intersections
**p=4.7e-3
Light
Dark
K
Norm entropy
**p=4.5e-3
*p=0.037
Norm complexity

Figure 12